UNIVERSITAT DE
BARCELONA

Development and optimization
of a Low Temperature Co-fired Ceramic suspension
for Mask-Image-Projection-based Stereolithography

Joana Gonçalves Fernandes

ANALYSIS OF MIP-SLA PRINTING PROCESS

CHAPTER IV

In this chapter the optimized LTCC suspension was used for the printing of the green body using the MIP-SLA machine. The influence of the layer thickness on the delamination of the green body was studied by varying the layer thickness. To evaluate the reproductivity along the whole printing area, the same piece was printed in a different position and the shrinkage and the excess of cure in the XY-plane is presented. For the resolution evaluation, cavities with different shapes and sizes were printed on the XY-plane and on the ZY- and ZX-planes. Moreover, some printing defects regarding both suspension formulation and printer characteristics are presented.

4.1. Introduction

The focus of this chapter is the printing process using the developed LTCC suspension. The additive manufacturing technology (AMT) used for this process was the Mask-Image-Projection-based Stereolithography (MIP-SLA). This 3D printer was developed by *Fundació privada centre CIM* (F-CIM) under the project *Nuevos procesos de impresión híbrida 3D/2D para dispositivos avanzados* (NHIBRID). Francisco Albero S.A.U (FAE) and Fundació Bosch i Gimpera- Universitat de Barcelona (FGB-UB) also participated in the development of this project, focused on the material formulation and characterization.

The MIP-SLA technology is based on the layer-by-layer principle, like other AMT. In this regard, the previous step of the printing process is the creation of a digital model, usually by a Computer-Aided Design (CAD) method. It is required in AM to convert the CAD model into a STL file which uses triangles to describe the surface of the object, without any representation of color, texture, or other common CAD model attributes. Once the STL file has been generated, the file is imported into a slicer program, slicing the 3D object into different layers.

Figure 4.1 shows the MIP-SLA printer, which has a top-down configuration. In this approach, the visible light projector is placed on the top and the building platform goes down during the printing process.
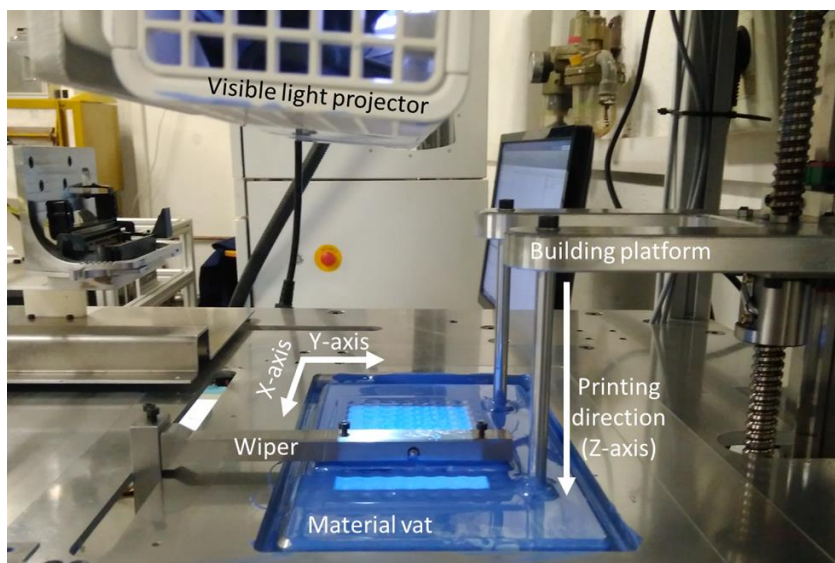
Figure 4.1 - MIP-SLA printer used for the printing of the green parts.

The main MIP-SLA components are identified in Figure 4.1: the visible light projector, building platform, wiper, and the vat which contains the resin. For further analysis, the XY-plane and the Z- axis are also identified in this image.

The printing process can be explained by five main steps, represented in Figure 4.2.
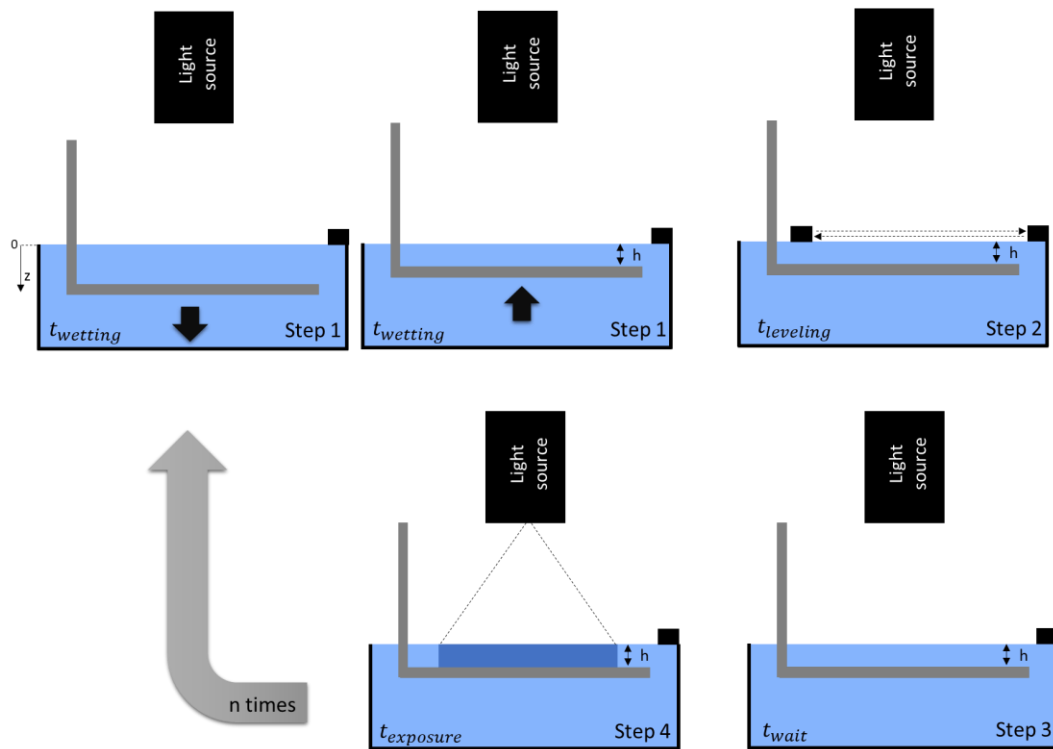
Figure 4.2 – Schematic of the printing process in the top-down MIP-SLA.

The zero of the Z-direction is placed at the top of the material vat. The first step of the printing process is the immersion of the building platform into the material vat. In this step the material recoats the building platform and then, the building platform is placed at a certain distance from its zero. This distance is one of the printing parameters, named layer thickness (h). Once the building platform is placed at the imposed layer thickness, in step 2 the wiper system levels the resin surface, ensuring a flat surface with the sample distance between the building platform and the resin surface. Before the curing of the layer, the printer remains at rest for a certain time, for the stress relaxation of the suspension. These three steps are denominated as the recoating process and are associated to a certain time:

$$t_{reacoating} = t_{wetting} + t_{leveling} + t_{wait} \qquad (equation\ 4.1)$$

Finally, the light projector projects one of the sliced layers, during a time, so-called the exposure time, $t_{exposure}$. This process is continually repeated for each layer. In this regard the time consumption per layer is given by:

$$t_{layer} = t_{wetting} + t_{leveling} + t_{wait} + t_{exposure} \qquad (equation\ 4.2)$$

Therefore, during the printing process the resin is cured, trapping the ceramic particles into the crosslinked resin matrix. At the end of this process the green body is obtained, i.e., the cured resin and the ceramic particles. After the printing process, the green bodies must be cleaned to remove the uncured suspension. In this work, all the printed pieces were cleaned with isopropanol and with air pressure, aiding the cleaning of small details. To obtain the final ceramic piece, the polymeric matrix must be eliminated by a thermal debinding process. Furthermore, the sintering of the debinded pieces is needed for its densifications. These steps will be discussed in the next chapter.

Before the printing process the SLT file must be sliced considering the layer thickness. Thus, the number of layers (n), and consequently the number of repetitions of the whole process, depends on the height of the 3D object (H) and the layer thickness, as shown in equation 4.3.

$$n = \frac{H}{h} \qquad (equation\ 4.3)$$

The layer thickness will affect the resolution in the Z-axis (printing direction) and the printing velocity. The lower the H, the higher the n, thus lowering the printing velocity. The printing velocity is determined by the number of layers required to build up a 3D printed object of a given height (H). The lower the layer thickness, the lower the printing velocity and the longer printing time required. Nevertheless, in contrast to the SLA where the polymerization is point by point, in MIP-SLA technology the time consumption to print one piece or a filled platform of pieces is exactly the same, since the photopolymerization process is layer-by-layer and not point by point.

In the MIP-SLA technology, the fabrication of each layer is made by curing the whole layer in contrast with the other AMTs which are point by point in each layer. Thus, the slicer of the SLT file results in several 2D images, one for each layer. These images are composed of white and black pixels with a certain area, depending on the 3D model. In the white areas the light can pass through, resulting in the curing of these areas. On the other hand, the black areas block the light from passing through them, thus the photopolymerization of the resin is inhibited.

The MIP-SLA machine uses a commercial Full HD Acer H6510BD projector, based on a DLP technology. The projector has a maximum resolution of 1920 x 1080 pixels (16:9), with a luminous flux of 3000 lm, using a 210 W lamp.

In the MIP-SLA printer, the distance between the visible light projector and the resin surface is closer in comparison to the experimental setup presented in the previous chapter. In this case the projected area is 122.5 X [122.5·(9/16)], which means an irradiance of I = 52 mW·cm^{-2}. This means that the resin receives an energy dose of 52 mJ·cm^{-2} for one second of exposure time. In this sense, the same exposure time does not result in the same energy dose in both systems (experimental setup and MIP-SLA machine), once the light projected is placed at different distances.

However, the main information for the printing process is the energy dose needed to apply to cure a certain cure depth. Then, this value could be converted into an exposure time taking into consideration the MIP-SLA configuration.

In this regard, the important data is the working curve of the optimized LTCC suspensions which were obtained in the previous chapter. Figure 4.3 shows the working curve, i.e., the cure depth as a function of the applied energy dose of the optimized LTCC suspension.

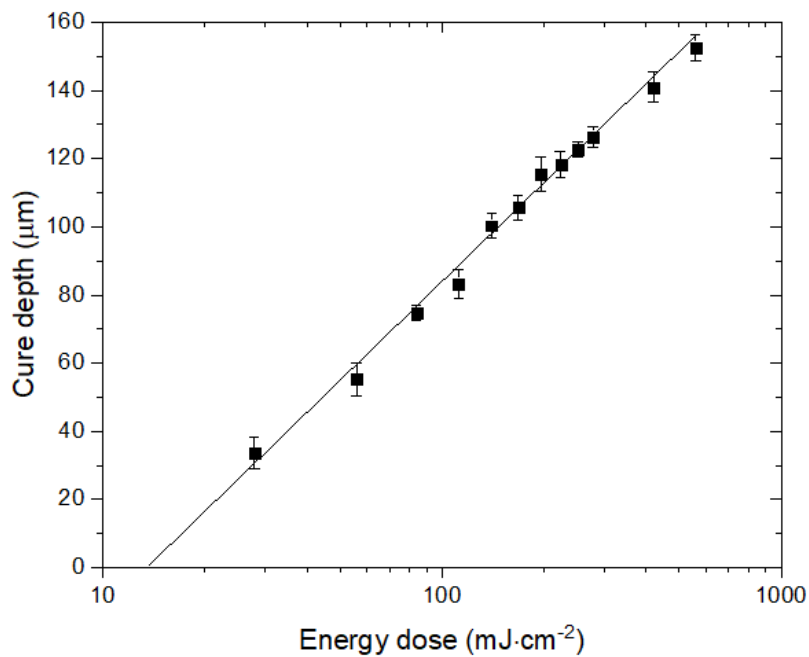*Figure 4.3 - Working curve of optimized 67 wt.% LTCC photocurable suspension.*

As a result, the energy dose to cure a certain cure depth, which is specific for each material, can be obtained from this curve. Figure 4.4 represents the relation between energy dose and exposure time, considering the projected area in the MIP-SLA printer.
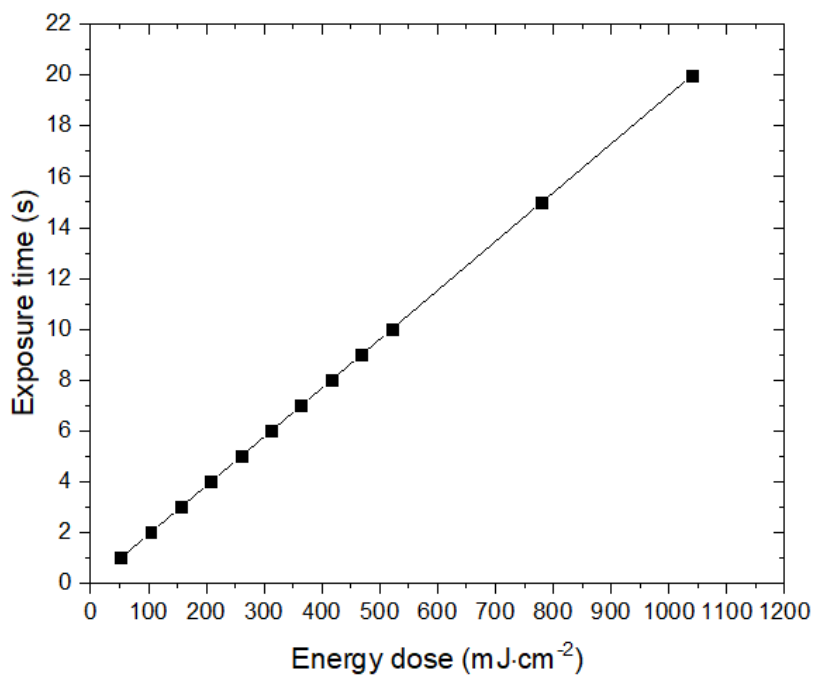

Figure 4.4 – Conversion of energy dose into exposure time.

This relationship is calculated from the multiplication of the irradiance (I = 52 mW·cm^{-2}) with the exposure time (in seconds), which gives the energy dose for a certain exposure time.

In this sense, the exposure time can be defined and specified for the printing process, considering the resultant cure depth. Note that this parameter is the time in which the light projector is projecting the 2D image for each layer.

Another important detail, which has not been discussed previously, is that the output of the projected light has an angle of 12 °. As the projection of each image (slice) is deflected 12°, a variation of both energy dose and angle of the incident light on the resin surface could be observed along the building area.

Note that the cure depth is the thickness which is cured when a certain energy dose is applied to the resin. On the other hand, the layer thickness is the parameter defined for the printing process. Accordingly, to successfully build a 3D-strucrure, the cure depth must be higher than the layer thickness, to overcure the n-1 layer, promoting the bonding of the layers.

In terms of the cured profile, in both SLA (laser spot) and MIP-SLA (pixel) technologies, the cured geometry does not have an ideal profile as shown in Figure 4.5. This can be explained due to the gaussian distribution of the energy light of the laser and the pixel. It is known that in the middle of the pixel or laser spot, the energy density is higher in comparison to the borders, thus the cured layer will have a gaussian-like profile, as shown in Figure 4.5 (real situation). [1]–[4]
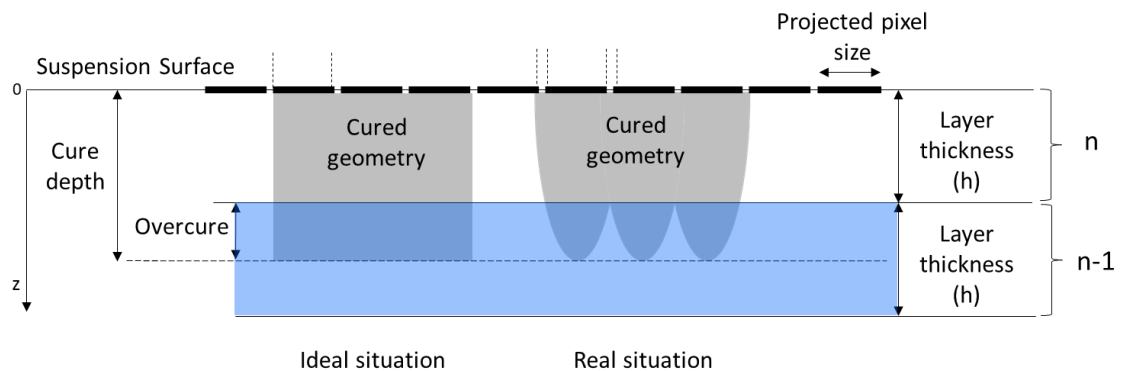

Figure 4.5 – Cured profile in an ideal and real situation.

119

Moreover, the degree of polymerization, or monomer conversion during the printing process, depends on the energy dose. In this regard, the monomer conversion can vary with depth, i.e., along the layer thickness. The monomer conversion increases with the applied energy dose. Therefore, the resultant polymer stiffens as the degree of polymerization increases. This variation in monomer conversion leads to a nonuniform cure profile.[3], [5] Furthermore, in a top-down configuration the oxygen inhibition in acrylates systems leads to incomplete curing and surface tackiness. [6]–[8]

In vat photopolymerization AM processes a nonuniform cure profile within each layer is observed. This nonuniformity may cause defects, such as cracking before or during thermal debinding. Hence, polymerization is accompanied by polymerization shrinkage. Defects such as delamination, distortions and bending in the green body can be formed due to the polymerization shrinkage, if a build style is inappropriate.[4], [6], [9]–[13][11] The technical data of the SPOT LV resin reports 6 % shrinkage during the photopolymerization.

For ceramic materials, it was demonstrated that the cure depth should be six times higher than the layer thickness to increase the bonding of the layers and, consequently, improves the debinding process.[9] This will be discussed in the next chapter.

As mentioned, the energy dose decreases along the layer thickness, i.e., the depth direction. The Beer-Lambert equation, equation 4.4, describes the variation of the energy dose along the depth direction, $E(z)$, depending on the applied energy, E_o, and the sensitivity in the depth direction, D_p.[5]

$$E(z) = E_o \cdot e^{\left(\frac{-Z}{D_p}\right)} \qquad (equation\ 4.4)$$

Note that the top surface of a cured layer has a maximum of polymerization. However, when $z > h$, the energy dose which travels this distance is not enough for the polymerization of the resin. This means that E (z>h) is lower than the critical energy dose, E_c, thus the polymerization does not occur. This factor must be considered when the layer thickness is defined for the printing process.

The polymerization stops when the energy dose is lower than the E_c. This effect also leads to the so-called print-through effect. This occurs when a suspended layer is printed and an unwanted solid is cured under the defined layer thickness, which degrades the fidelity of the build. [5]This effect will be further discussed during this chapter.

Another factor is the scattering of the light by the LTCC particle. During the photopolymerization process, this phenomenon is observed when the 2D image is projected and cures the LTCC suspensions. This effect was analyzed in the previous chapter, where it was concluded that the solid load decreases the cured depth (z-direction) due to the scattering of the light. In addition, the light scattering effect is also observed in the XY-plane. In this case, an excess of cured area is detected, i.e., an increase of the cured area with respect to the projected one.

The resin, which is cured due to the scattering of the light in the XY-plane, is called excess width (W_{ex}). The W_{ex}, due to the broadening, is defined as one-half the difference between the measured line width (W) and the projected width ($W_{illumination}$), as shown in equation 4.5.[5]

$$W_{ex} = \frac{|w - w_{illumination}|}{2} \qquad (equation\ 4.5)$$

Figure 4.6 shows an example of the light scattering effect in two different situations. Note that the black and white image represents the projected 2D image and the blue ones represent the resulting cured resin. If these images are projected at each layer, the 3D object obtained after the printing process will be a cylinder, for Figure 4.6a, and a cube with a cylindrical cavity in the case of Figure 4.6.b.
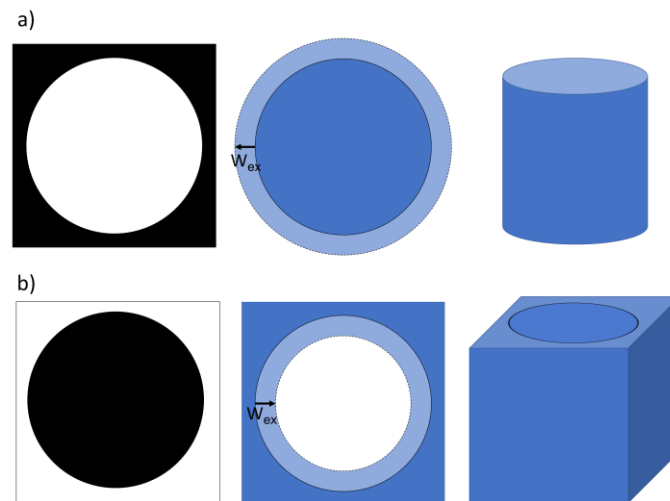
Figure 4.6 – a) Printing of a cylinder b) printing of a cube with a circular cavity. Black and white images correspond to the slice image; blue images represent the dimensional variation due to the scattering of light.

Regarding the excess width, in Figure 4.6.a, the cylinder will have a higher diameter. However, in the second case the cavity will have a smaller diameter and the whole cube will have a higher dimension. This effect increases as the energy dose increases. Thus, the higher the exposure time the higher the excess width. This directly affects the XY-resolution and consequently a correct geometry transfer.

To bond the different layers along the printing piece properly, a high value of cure depth is needed. For this to happen, a high energy dose must by applied to the resin, resulting in a worse XY resolution because of the scattering of the light by the ceramic particles.

Apart from the scattering effect, the XY-resolution is also affected by the characteristics of the light source, such as the pixel size of the digital micromirror device (DMD) presented in the DLP-based projector and the distance between the projector and the resin surface. Accordingly, the printing area and the XY-resolution are both correlated, i.e., the distance between the projector and the resin surface will affect both parameters. To summarize, the closer the distance the higher the resolution, but the smaller the printing area.

This distance was kept constant during all printings. As said before, the projected area is 122.5 x 68.9 mm^2, which translates to a theoretical XY-resolution of 63.8 μm (side length) of the projected pixel. This result is based on the resolution of the projector, which is 1920 x 1080 pixels. However, there is a scattering of the light which leads to a broadening of the projected shape, decreasing the resolution in the XY-plane.

On the other hand, the Z-resolution is determined by the layer thickness (h). The minimum height in the building direction (Z-axis) in the developed MIP-SLA machine is 12.5 μm, theoretically. This resolution is given by the resolution of the motor of the building platform.

The typical layer thickness used for the printing process for ceramic pieces ranges between 25 and 250 μm. As stated, thinner layers allow for more detail and more accurate resolution in the printing direction (z-axis), however with higher time consumption, since each layer takes a certain time for the recoating and photopolymerization steps.[5], [14]

In a top-down configuration system, the platform is immersed into the resin vat during the printing process. Moreover, the support structure of the building platform also dips into the resin during the printing process, increasing the immersed volume. Accordingly, a wiper has been added to the MIP-SLA machine to ensure the homogeneity and the leveling of the recoated layer. In the recoating step, the excess of resin by the immersion of the parts is poured out into a channel that surrounds the vat.

The velocity of the recoating system and the rheological properties of the suspensions are important parameters for the deposition of each layer. The values of shear rates (γ̇) applied to the resin during the recoating step are related to the velocity of the recoating unit and the layer thickness (h), through the following relationship:

$$\dot{\gamma} = \frac{\text{wiper velocity}}{\text{h}} \qquad\qquad (equation\ 4.6)$$
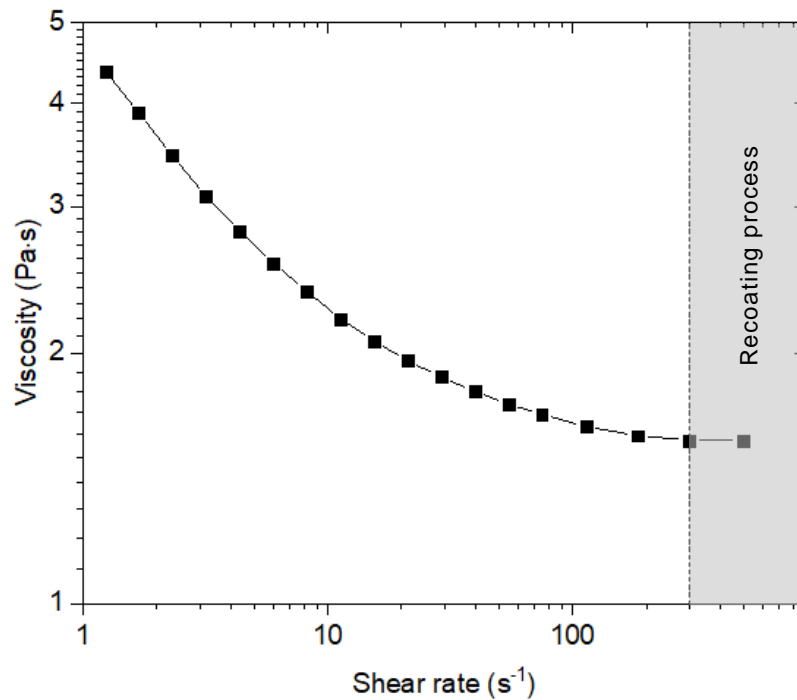
Figure 4.7 – Flow curve of the optimized 67 wt.% LTCC photocurable suspension.

The flow curve of the optimized LTCC photocurable suspension is presented in Figure 4.7. It is observed that the viscosity tends to a constant value for shear rates higher than 300 s^{-1}, with a viscosity value of 1.6 Pa·s.

In this sense, it is convenient that the recoating system works at shear rates greater than 300 s^{-1}, which corresponds to the lowest viscosity, aiding the homogenization of the recoated layer.

Once the printing of the green parts was performed from 12.5 to 75 μm of layer thickness, the recoating velocity must be at least 3.75 mm·s^{-1} for the printing of pieces with h =12.5 μm and 22.5 mm·s^{-1} for the ones printed with h =75 μm. This parameter was kept constant during the entire experiment, with a value of 25 mm·s^{-1}. This ensures that in all cases the recoating system is performed with a shear rate higher than 300 s^{-1}.

4.2. Printing features

In this section the printing features are analyzed for the developed LTCC suspension, and a study of printing at different layer thicknesses is realized, regarding the resolution in both the XY-plane and Z-direction. Moreover, the differences along the printing area will be discussed, defining the zones with the highest printing fidelity and accuracy.

4.2.1. Influence of layer thickness and cure depth

This study's main objective is to analyze the relationship between the layer thickness (h)and the cure depth (C_d), on the defects of the final pieces after the debinding and sintering processes. In this section only the green body results are shown, which will serve for further analysis presented in the following chapter.

As said previously, the applied energy dose corresponds to a certain value of C_d. This relationship is presented in Figure 4.3 for the optimized LTCC suspension. Thus, for an energy dose of 520 mJ·cm^{-2}, a C_d of 150 μm is obtained. From Figure 4.4, the energy doses can be converted into the exposure time, i.e., 10 seconds of exposure time is required to irradiate an energy dose of 520 mJ·cm^{-2}.

The profile of the energy dose along the Z-axis of the cured LTCC suspension can be expressed as a function of the applied energy dose and the sensitivity of the suspension (see equation 4.4).

Figure 4.8 shows the energy dose profile when an energy dose of 520 mJ·cm^{-2}is applied to the LTCC suspension which has a D_p of 41 μm. The critical energy dose (E_c =14 mJ·cm^{-2}) of the LTCC suspension is also presented in this graphic, which is the minimum energy dose required to initiate the photopolymerization process. Both sensitivity and critical energy dose of the optimized LTCC suspension were characterized in the previous chapter. Moreover, sensitivity and attenuation factor are both correlated: the attenuation factor is the inverse of the sensitivity. In this experiment the same energy dose was applied during printing, varying the layer thickness of the printed pieces.
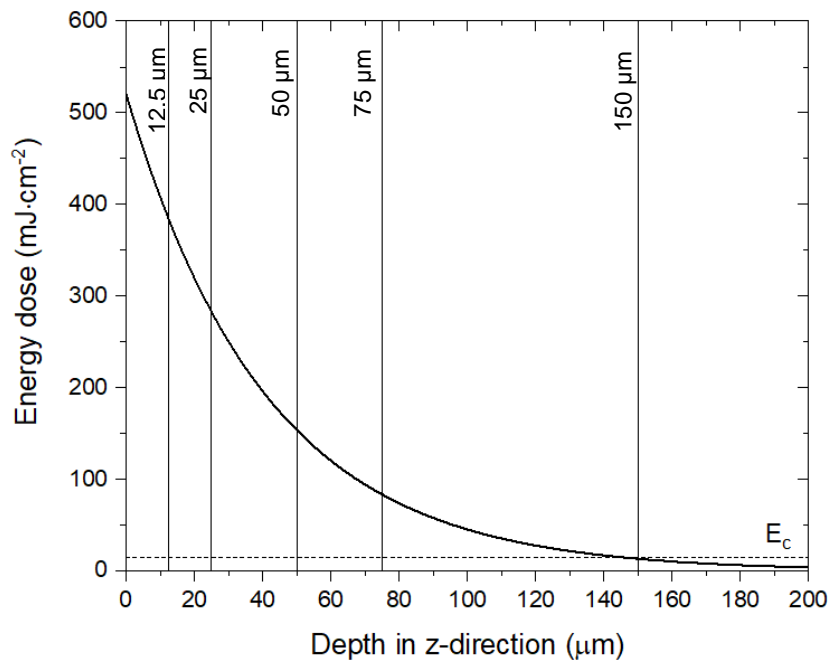
Figure 4.8 – Energy dose profile along the Z-direction for incident energy dose of 520 mJ·cm⁻².

The layer thicknesses used for the printing of the different pieces were 12.5, 25, 50, and 75 μm, which are represented in Figure 4.8. Note that the zero in the Z-direction corresponds to the top of the layer thickness, which corresponds to the maximum energy dose, i.e., the applied one (520 mJ·cm^{-2}). As expected, the energy dose decreases along the Z-direction, due to the attenuation of the light by the ceramic particles. In this regard, the layer thickness presents a cure profile, since the polymerization degree depends on the energy dose. This graded cure profile is more evident as the layer thickness increases. For h=12.5 μm the energy that reaches the bottom of the layer is 385 mJ·cm^{-2}, however for h=75 μm the energy dose is 83 mJ·cm^{-2} at the bottom of the layer.

In addition, this means that the overcure of the n-x (x=1,2,3…) layer is different depending on the layer thickness. For example, in the case of h=25 μm, the energy dose overcures the five layers above, assuming the same value of attenuation factor of the uncured suspension as for the cured suspension.

As h increases, the number of overcured layers decreases, reaching $h=C_d$ at 150 μm, where the n-1 layer is not overcured. In this extreme case, the layers are not bonded, making the 3D printing process impossible.

For this study, different batches of six pieces were printed with different layer thicknesses: 12.5, 25, 50, and 75 μm, with the same exposure time of 10 seconds. For this study, a simple geometry was chosen to simplify its analysis. The selected geometry was a cylinder with a diameter of 10 mm, a height of 5 mm, and a wall thickness of 2 mm, as shown in Figure 4.9.
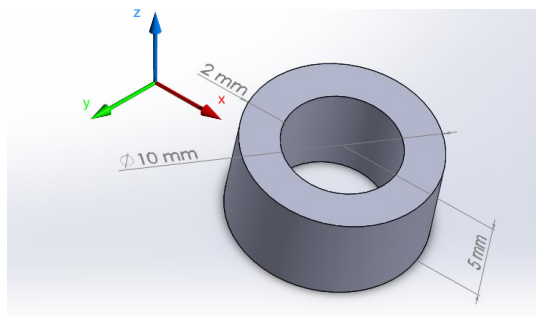

Figure 4.9 – Dimension of the cylinder.

Figure 4.10 shows the vat with the LTCC suspensions during the printing process of the cylinders. The printing process is done by projecting all of the layer, not point by point. Thus, in MIP-SLA technology the printing process does not depend on the number of parts.
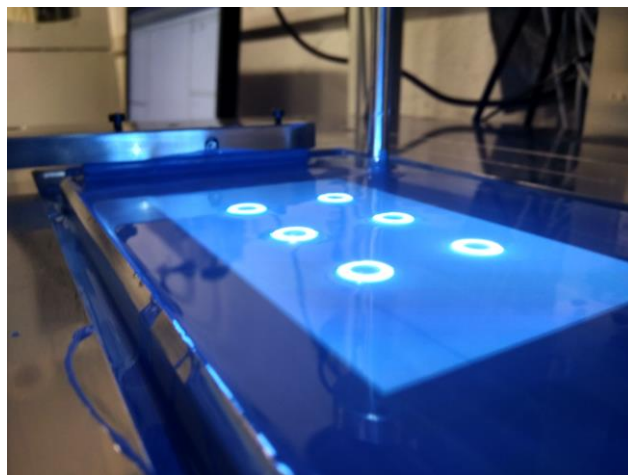

Figure 4.10 – Curing of one layer during the printing of the cylinders.

After the printing process, all samples were cleaned with isopropanol and with air pressure to remove the uncured suspension.

The dimensions of the cylinders were measured after the cleaning process, in both the Z-direction and XY-plane. Table 4.1 shows the percentage variation with respect to the CAD model.

Table 4.1 – Dimensional variation of the green bodies in the Z-direction and XY-plane with different layer thicknesses.

Layer thickness (µm)	Z-axis variation (%)	XY- plane variation (%)
12.5	-	-2.8 ± 1.6
25.0	+ 10.5 ± 2.6	-2.6 ± 1.1
50.0	+ 11.6 ± 2.3	-2.2 ± 0.9
75.0	+ 8.4 ± 2.7	-2.6 ± 1.1

It is observed that in all the cases there is a shrinkage of 2-3 % in the XY-plane, with no correlation with the layer thickness. It is known that the polymerization of the resin results in a shrinkage. Additionally, the light scattering leads to an overgrowth (excess width) in the XY-plane. Thus, both phenomena result in an opposite dimensional variation of the whole pieces., i.e., the polymerization causes a size reduction, and, on the other hand, the excess width causes an increase in the dimensions.

However, a shrinkage in the XY-plane is observed. This means that the shrinkage effect predominates during the printing process, masking the overgrowth due to the scattering of light.

Regarding the Z-axis, an overgrowth is observed for all samples. This effect will be discussed later in the printing defects section.

Figure 4.11 shows the SEM images of the printed cylinders at different layer thicknesses. These images are related to z-resolution which corresponds to the printing direction.
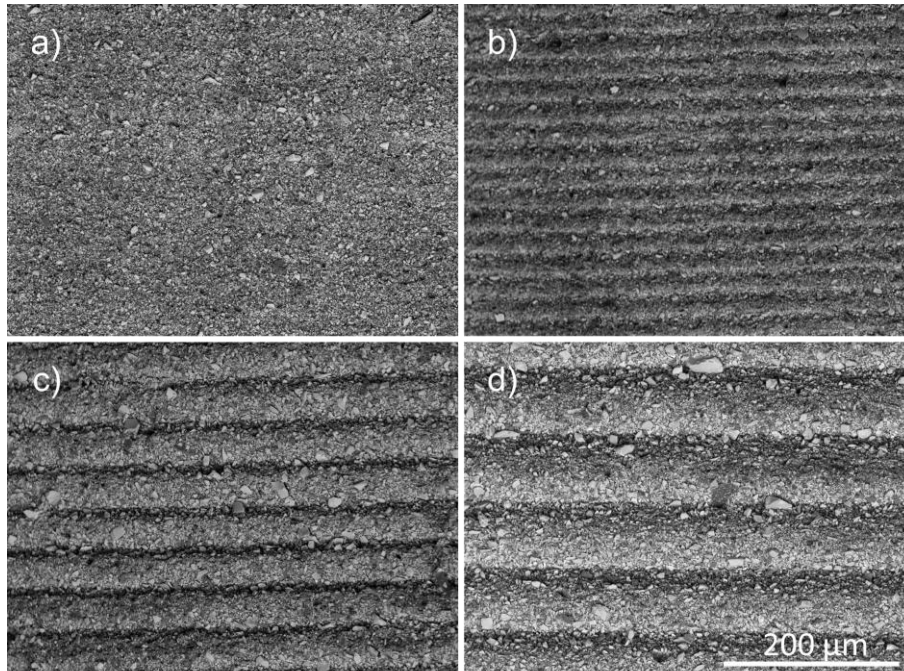
Figure 4.11 – Backscattered electron images of the green bodies along the z-direction, printed with the same energy dose at different layer thicknesses a) 12.5 μm b) 25 μm c) 50 μm and d) 75 μm. (images have the same magnification).

The layer thicknesses can be clearly identified for 25, 50, and 75 μm. Nevertheless, in the case of 12.5 μm layer thickness, it is not possible to distinguish them. The results show an average of 25 ± 2 μm, 48 ± 3 μm, and 73 ± 3 μm, for the layer thicknesses of 25 μm, 50 μm, and 75 μm, respectively.

For a better understanding of the printing process, the previous samples were sectioned along the printing direction. Figure 4.12 shows the cross-section (perpendicular to the XY-plane) of the previous samples.
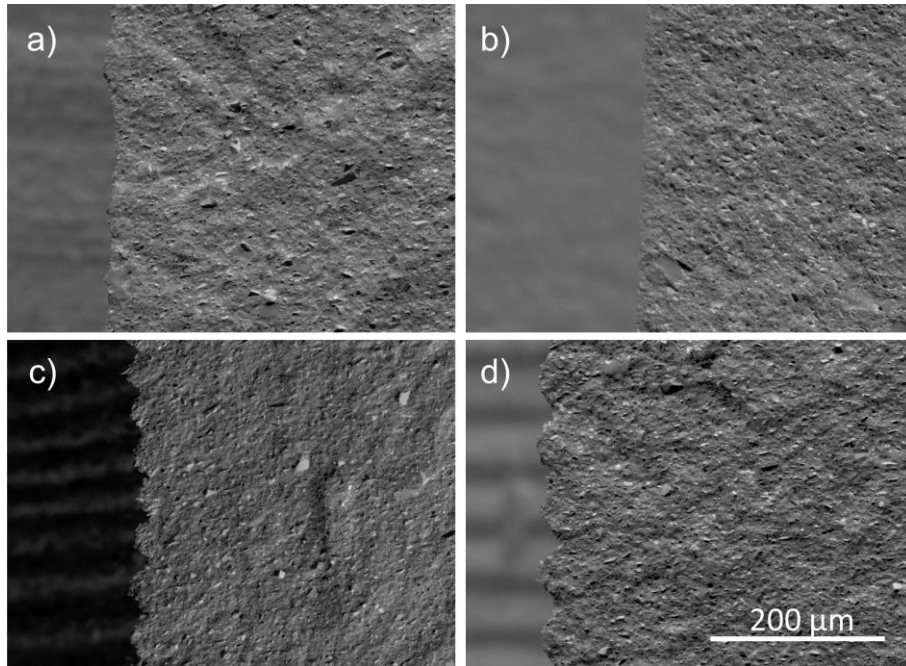
Figure 4.12 –Backscattered electron images of the cross-section of the green bodies printed with the same energy dose at different layer thicknesses a) 12.5 µm b) 25 µm c) 50 µm and d) 75 µm. (images have the same magnification).

A wave-like effect at the surface is observed, due to the layer-by-layer building process. This effect is more evident for the pieces printed at h=50 µm and h=75 µm. However, the interior of the pieces presents a homogenous surface, thus, the layers could not be identified and no evidence of delamination between layers is observed.

For a deeper observation, x-ray image analysis was performed on the different samples. This is a non-destructive technique which allows for the observation of the whole piece. In this sense, it is used to inspect if there is some internal defect, such as delamination or air bubbles inside the green body. Figure 4.13 shows the X-ray images for the samples printed at different layer thicknesses.
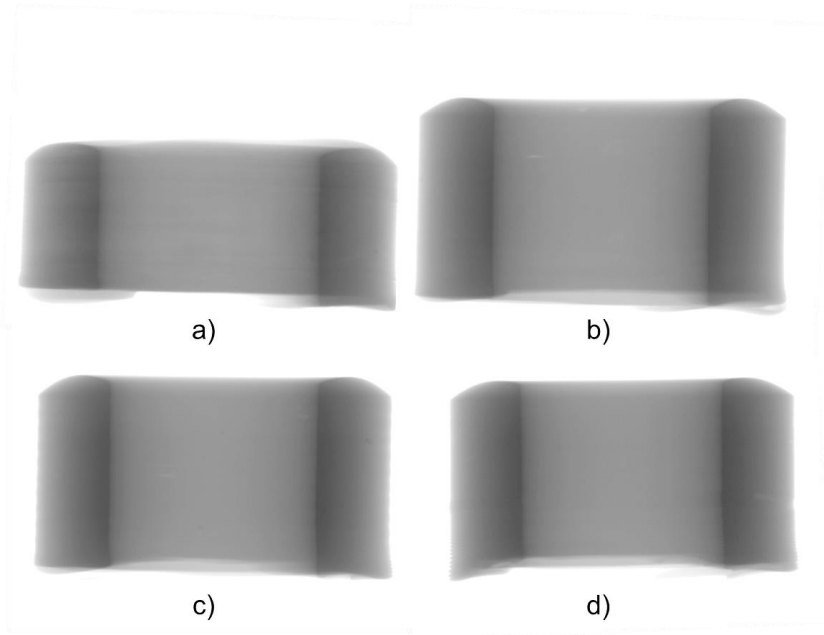
Figure 4.13 - X-ray images of the green bodies printed at different layer thicknesses a) 12.5 μm b) 25 μm c) 50 μm and d) 75 μm with the same energy dose.

Analyzing the results, there is no evidence of delamination or major defect in any of the cylinders. However, during the printing process of the samples with h=12.5 μm, an excessive overgrowth is observed after a certain number of printed layers. Because of this excessive overgrowth, the wiper impacts on the green body and, consequently, the printing process cannot be completed, as shown in Figure 4.13.a.Thus, it can be concluded that the minimum layer thickness is 25 μm, limiting the z-resolution.

4.2.2. Analysis of printing area

As mentioned previously, in the MIP-SLA technology the distance between the light projector and the resin surface determines the projected area and its resolution. However, the complete parallelism of the light projector and the resin surface is technically difficult. Moreover, the focus of the light projector at the resin level is a manual procedure, which could affect the printing resolution. Apart from these two factors, it is known that the light is projected with a projection angle of 12°, meaning that the focus of the projected slice is not the same along the printing area.

In this regard, it is important to know how these setup characteristics affect the printed green bodies. To evaluate the homogeneity of the whole available printing area, the same geometry was printed in different positions. Figure 4.14 shows the CAD of the whole pieces, placed along the printing platform. These pieces were defined with circular and quadrangular cavities to evaluate the accuracy on the pattern transfer, over all the printing area. The axes are identified in Figure 4.14, where the z-axis corresponds to the printing direction.
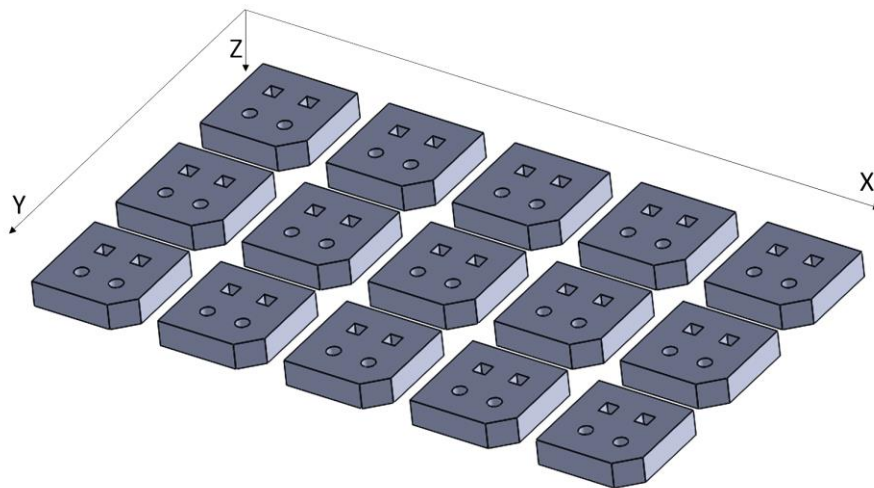

Figure 4.14 – CAD and piece distribution of the printing area experiment

The STL files were sliced, generating the 2D images which are projected during the printing process at each layer.

The printing process was performed at h=50 µm with 10 seconds of exposure time (C_d =150 µm) in all cases. The piece's height is 4 mm, therefore the resulting number of slices/layers is 80. Fifteen pieces were distributed over the printing area defined in Figure 4.15.

In this geometry, two different images are projected along the printing process, shown in Figure 4.15.b. The first 40 layers were printed without the cavities (completely white image) and the last 40 layers with the cavities. The main dimensions are expressed in pixels, which serves for further analysis.
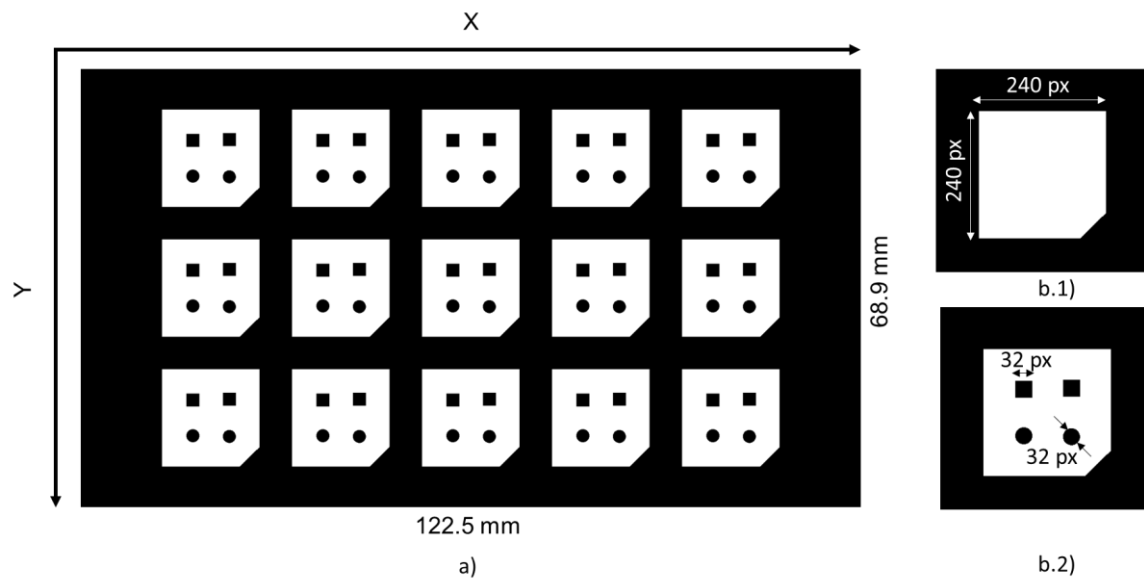
Figure 4.15 – a) Slice dimension of the printed area with all the pieces and b) dimensions of the individual printed piece: b.1 - the first 40 layers without cavities and b.2 - the last 40 layers with the cavities.

In this study, all the cavities were measured and compared with the slice file, as well as the external dimensions of the pieces. In the quadrangular cavities, the dimensions were measured in the X-axis and Y-axis to see if there are dimensional differences in the XY-plane. Additionally, the circularity of the circular cavities was evaluated. The dimensional variation of the external dimensions was measured in the 3 dimensions (x, y, and z-axis).

For this study it is important to know the number of pixels projected for each element, which can be obtained by the slice image. As previously described, each projected pixel has a side measuring 63.8 µm, thus the cavities have 2041.6 µm sides and/or diameters (32 pixels x 63.8 µm). The external dimensions of the XY-plane of each piece is 240 x 240 pixels, which means 15.312 mm side.

For the analysis, a matrix of rows and columns was defined. The letters A, B, and C correspond to the rows (Y-axis) and 1 to 5 to the columns (X-axis). Figure 4.16 shows the projection of the slice presented in Figure 4.15 and Figure 4.16b the final printed parts with the defined matrix.
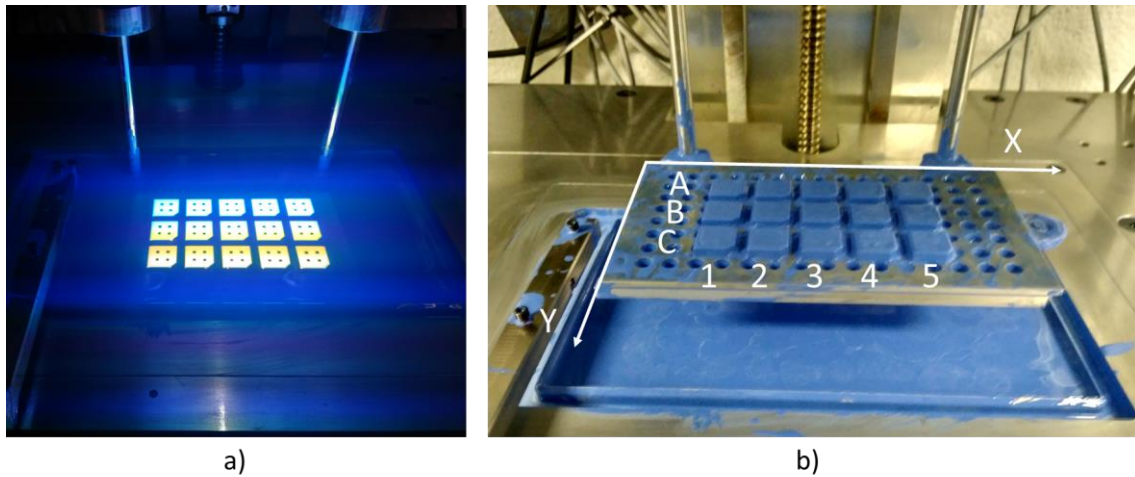
Figure 4.16 – a) Projected image of the last 40 layers and b) the pieces after the printing process with defined matrix in the XY-plane.

A detail of the CAD model and the green printed piece is presented in Figure 4.17.
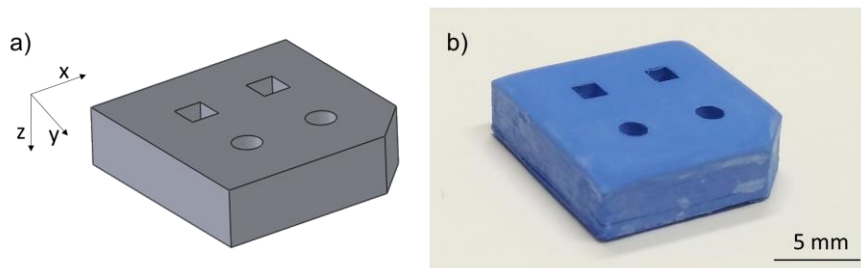
Figure 4.17 – a) CAD model piece and b) green printed piece.

As mentioned, during the printing process both phenomena are involved: shrinkage due to the polymerization and curing excess in the XY-plane due to the scattering of the light by the ceramic particles. As in the previous results, a shrinkage in the XY-plane was observed. Thus, the shrinkage of the pieces presents a higher influence on dimensional variation in the XY-plane, as expected.

In this study, the X-axis and Y-axis shrinkages were analyzed independently, showing different values of shrinkage. A shrinkage of 1.8 ± 0.8 % was observed for the X-axis and 2.9 ± 0.7 % in the Y-axis. Regarding the Z-axis, it is expected that the shrinkage by the polymerization of the pieces should occur for the whole volume. However, an overgrowth in the Z-axis was observed with dimensions of 10 ± 0.8 %, as in the previous study. This effect will be explained in the printing defects section. Figure 4.18 shows a scheme of the dimensional variations observed in the external dimensions in the XY-plane and Z-direction.
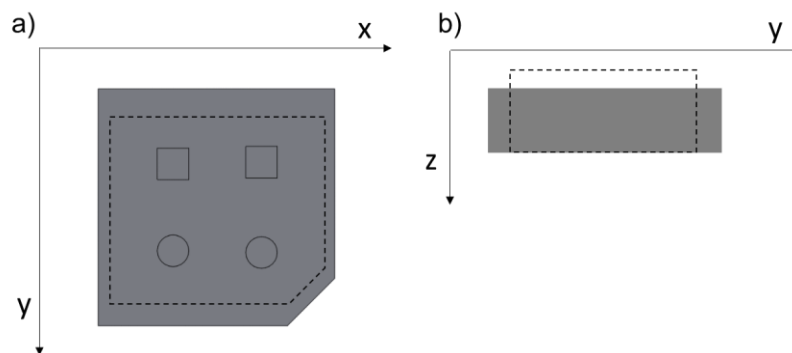
Figure 4.18 – Scheme of the shrinkage of the a) XY-plane and b) the overgrowth in the Z-axis.

The shrinkage differences observed in the X-axis and Y-axis could be explained by[1], [3]:

(1) non-homogeneity of the energy distribution of the pixel in both axes, which leads to the different polymerization degrees, thus different shrinkages.

(2) distortion of the projected pixel dimensions.

Apart from the dimensional variation of the whole pieces, the cavities printed on the top of the pieces were also studied in both the X-axis and Y-axis directions. Note that the shrinkage observed previously of the whole piece will also affect the dimensions of the cavities (reducing their size). However, in this study the effect of the scattering can be evaluated once the shrinkage and the excess width (W_{ex}) present the same direction. Figure 4.19 shows the effect of the shrinkage and the W_{ex} on the size variation of the cavities.
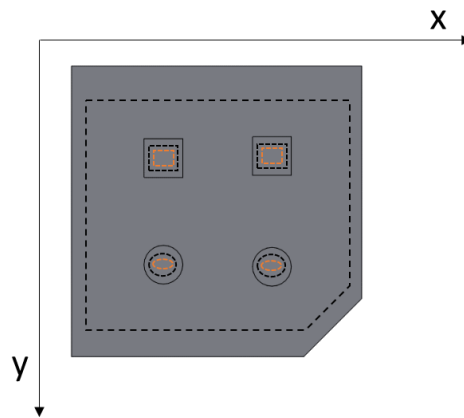
Figure 4.19 – Dimensional reduction due to the shrinkage (black dotted lines) and due to the W_{ex} (orange dotted lines).

Knowing the whole shrinkage values in the X and Y axes for each piece, which were calculated in the previous study, the contribution of the W_{ex} can be calculated.

These cavities were analyzed by optical microscope image, measuring the final dimensions of the cavities to compare with the slice dimensions. The presented results take into consideration the X and Y-axes shrinkage, meaning that the results show the contribution of the W_{ex} on the cavity size variation.

In this sense, in the following results the percentage of shrinkage measured in the X and Y-axes were subtracted, i.e., if the projected image is 2041.6 µm (32 pixels), the reference value for this study is 2041.6 µm minus the corresponding percentage of shrinkage.

The following results demonstrate the size reduction of the quadrangular cavities due to the light scattering, which leads to a curing excess, reducing the size of the cavity. Figure 4.20 displays the W_{ex} in the X-axis for the different pieces placed along the building platform.

Figure 4.20 - Dimensional variation measured in the X-axis of the quadrangular cavities for all printed pieces along the printing area

In the X-axis, the W_{ex} presents a variation of 90 μm [60-150 ± 10 μm] along the printing area, where the higher values correspond to the right zone. Figure 4.21 shows the W_{ex} measured on the quadrangular cavities in the Y-axis for all printed samples.
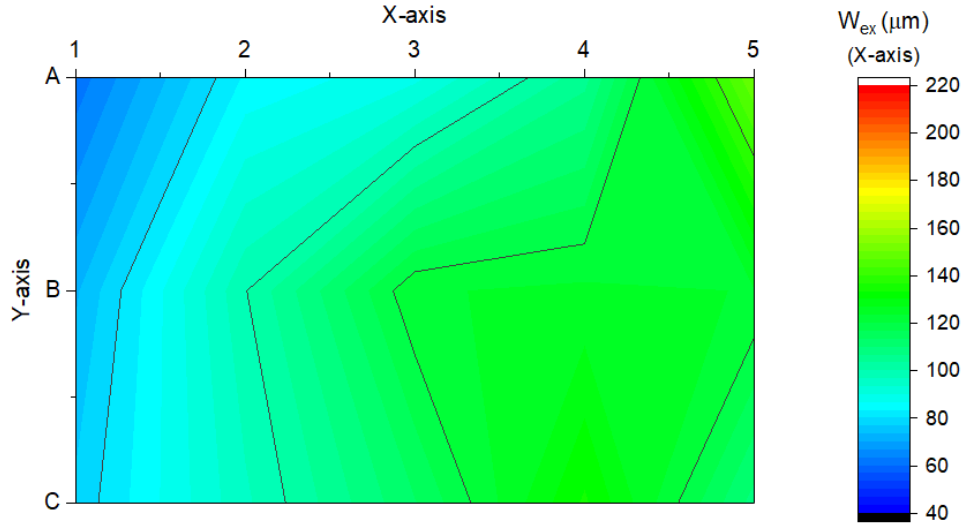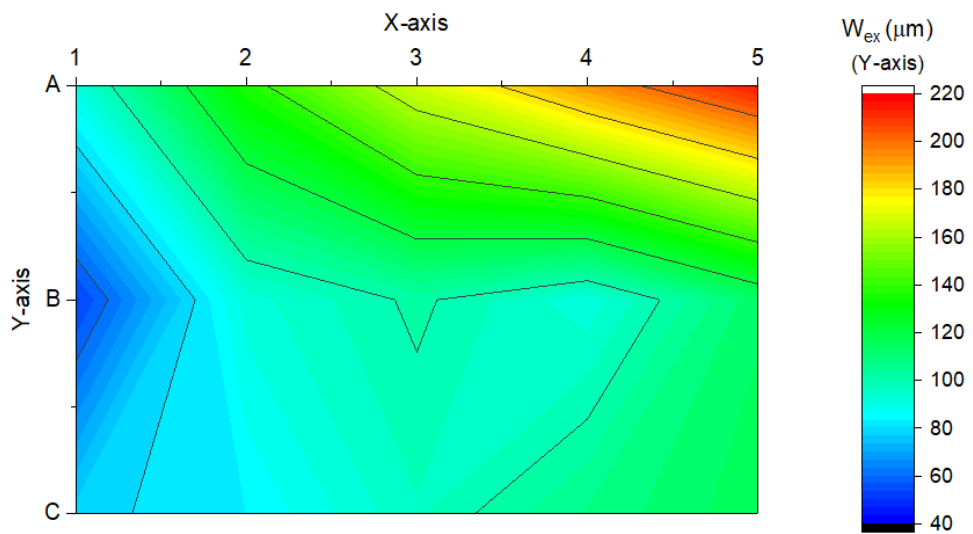

Figure 4.21 - Dimensional variation measured in the Y-axis of the quadrangular cavities for all printed pieces along the printing area.

In this case the W_{ex} presents a higher variation than the X-axis, with a value of 166 µm [50-215 ± 10 µm]. The highest variation is placed in the top right of the printing area.

Theoretically, the incident light has an energy dose of 520 mJ·cm^{-2} (10 seconds of exposure time) over the printing area. Nevertheless, this value is an ideal case, where the light path has the same length at all points of the building platform. As the output of the projected light has an angle of 12°, the path length of the light is not the same at all points of the printing area, varying the energy dose. Another factor is the focal distance, since not all the points have the same focal distance, i.e., not all the points are equally focused. Moreover, the incident light beam has different angles along the printing area. A scheme of the light projection in the MIP-SLA printer is presented in Figure 4.22, where it is observed that the light path and its inclination is not the same along projected area.
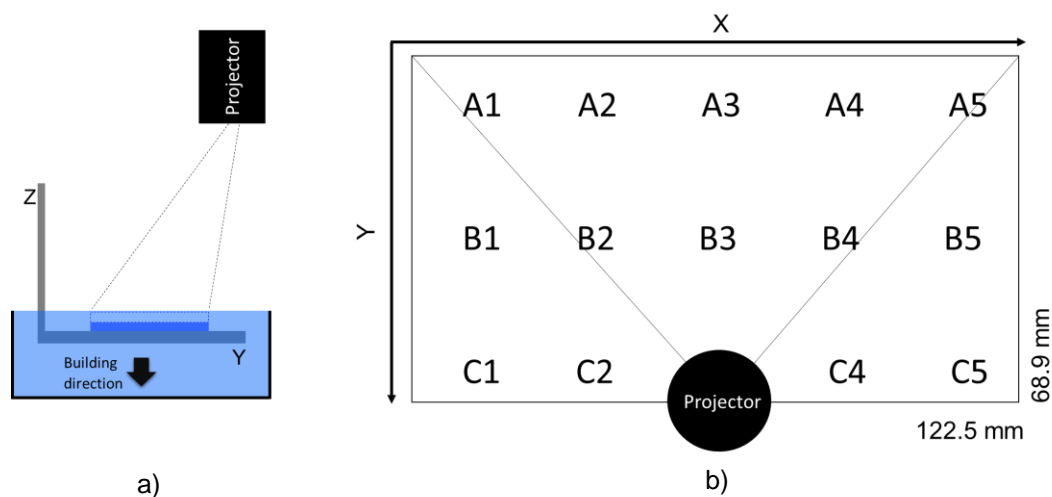
Figure 4.22 – Light projection in the MIP-SLA printer a) lateral view and b) top view.

Taking into consideration the projection profile of the light, and assuming a perfect parallelism between the LTCC suspension surface and the projector, a lower energy dose should reach the A row than the B and C rows. Therefore, the W_{ex} should be lower in the A row. Nevertheless, it was found that the area with the highest W_{ex} is in the A5 position, for both the X and Y-directions. This is explained due to the non-parallelism between the resin surface and the projector.

In other words, in a top-down MIP-SLA configuration, the resin distribution along the printing area always has the same level, once it is controlled by gravity forces. In this sense, the observed variation of the W_{ex} is explained by the projector alignment, which is not totally parallel to the resin surface, or even by a lens distortion.

Thus, a variation of the values of W_{ex} is observed because the energy dose is not uniformly distributed over the printing area due to the projection itself and the parallelism between the projector and the suspension surface.

Another consideration to take into account is that the W_{ex} variation is higher in the Y-axis than in the X-axis. This effect is explained by a nonuniformity of the light intensity inside the pixels and/or a dimensional distortion of the pixel. Since the value of W_{ex} is higher in the Y-axis, this means that the energy dose is higher in this direction of the pixel and/or the Y-side of the pixel is smaller in comparison with the X-side. Note that in the X-axis the highest W_{ex} is 150 µm and the highest in the Y-axis is 215 µm, both placed in the A5 position.

If the energy distribution along the Y-axis of the pixel is higher than in the X-axis, a higher shrinkage occurs during the polymerization in the Y-axis. On the other hand, if the size of the projected pixel is not the same in both sides, it means that a rectangular pixel is projected and affects the whole dimension of the projected image. This effect justifies the differences in the shrinkage in the X and Y-axes of the whole pieces. As seen previously, the Y-axis presented the higher dimensional variation.

The circularity of the circular cavities was also studied using the ImageJ program by adjusting a circle to the circular cavity. The results are presented in terms of percentage, between 0 and 100 %, where 100 % indicates a perfect circle and, as the percentage decreases, the shape presents a more ellipse-like shape (Figure 4.23).
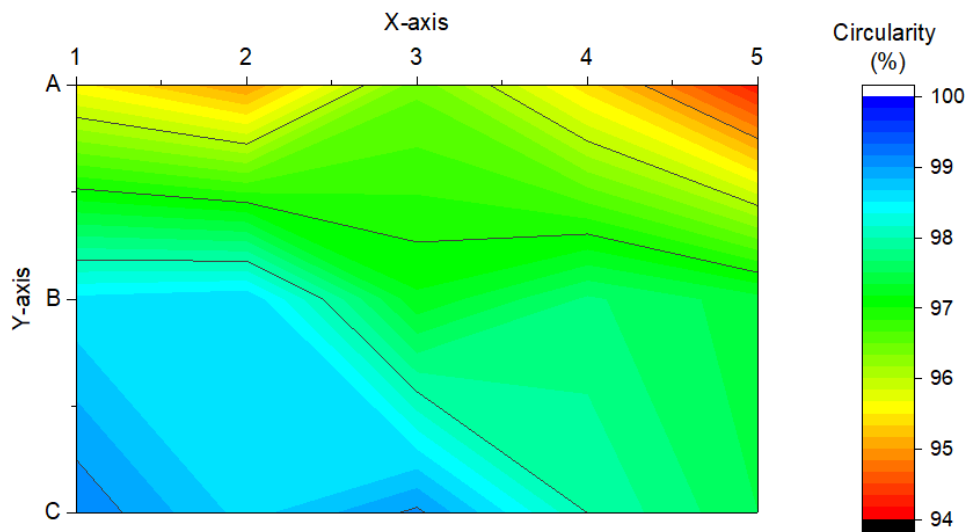
Figure 4.23 –Circularity percentage of the circular cavities.

The printing area with the highest circularity is the bottom-left (C1 position), and the lowest circularity is placed in the top zone.

So far, just the W_{ex} has been analyzed for both types of cavities. However, both effects, shrinkage and W_{ex}, affect the accuracy of the final printed patterns. To better understand both effects at the same time, an overall analysis of the dimensional variation is presented for the quadrangular cavities. Figure 4.24 represents the percentage differences between
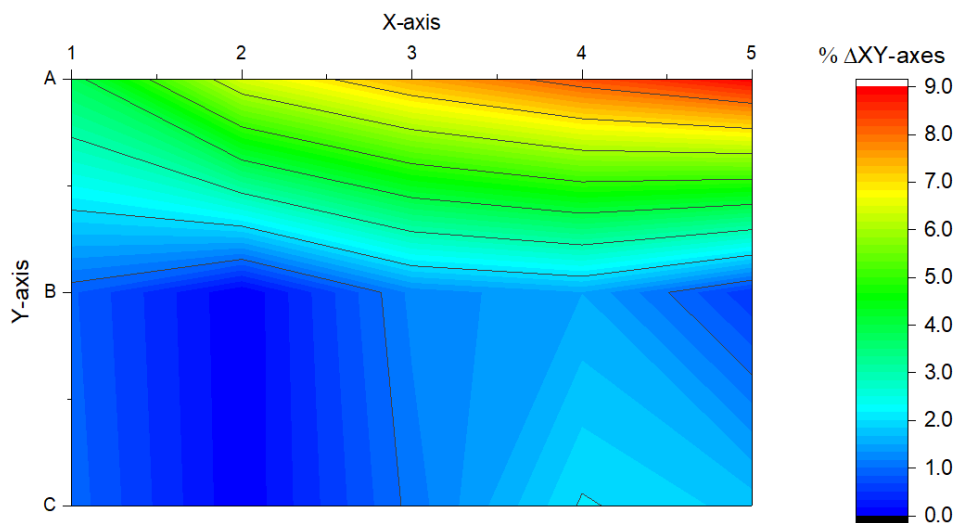
Figure 4.24 – Dimension variation of the X and Y-axes considering the shrinkage and W_{ex}.

the X-axis and Y-axis dimensional variation for the quadrangular cavities, considering both phenomena.

Analyzing Figure 4.24, the lowest differences in the size variation in the X and Y-axes are placed at the bottom of the printing area. Regarding the circularity, if the X and Y-axis present the same dimensional variation, the circular cavities have a high value of circularity, once the overall size variation is similar in both directions. Therefore, the lowest difference between the X and Y-axes, the better the circularity. As a result, the most accurate zone is placed also in the bottom of the printing area in Figure 4.23.

Figure 4.25 shows an image during the printing process, identifying the pieces with the highest and lowest dimensional distortions, A5 and C1, respectively.
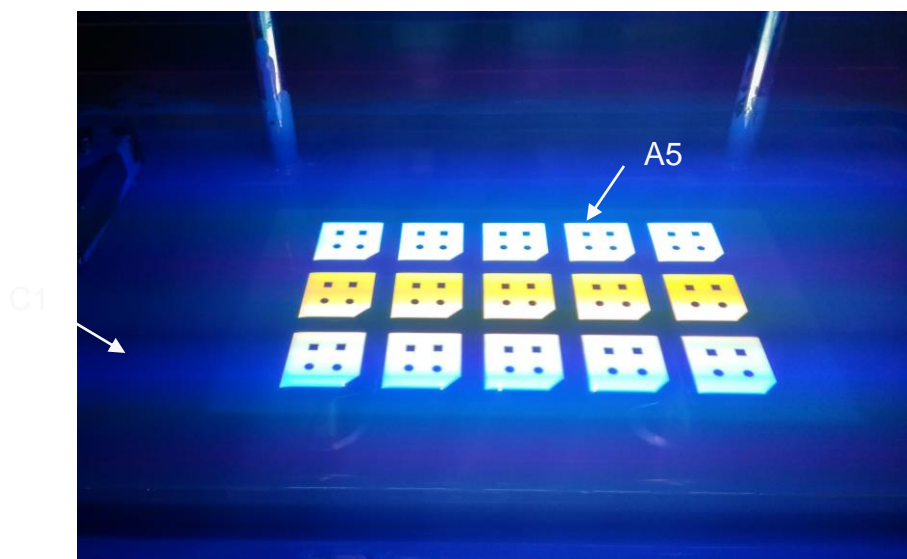
Figure 4.25 – Piece identification with the highest dimensional distortion, A5, and the lowest dimensional distortion, C1.

Figure 4.26 presents the slice image on the quadrangular and circular cavities, with the black and white pixels. For the quadrangular cavities a grind of 32 pixels by side blocks the light from passing through for the printing of the cavity. The black pixels for the circular cavities present a circular grid with a diameter of 32 pixels.

141
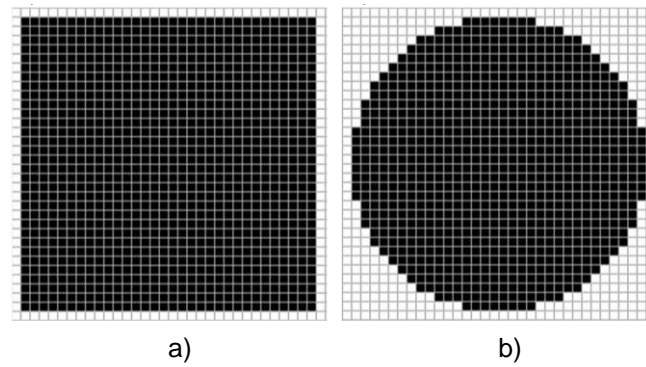
Figure 4.26 –Slice image of the a) quadrangular cavity and b) circular cavity.

The optical analysis of the quadrangular and circular cavities of the two samples, A5 and C1, was carried out (Figure 4.27). A grid of pixels is presented overlapping the optical images for a better visualization of the dimensional variation. The grids are the same as the ones shown in Figure 4.26, but in this case the black pixels are transparent to analyze the images placed below it. The presented grid is 32 x 32 pixels with a side of 63.8 μm for the quadrangular cavities and with a 32 pixel diameter with a side of 63.8 μm for the circular ones.
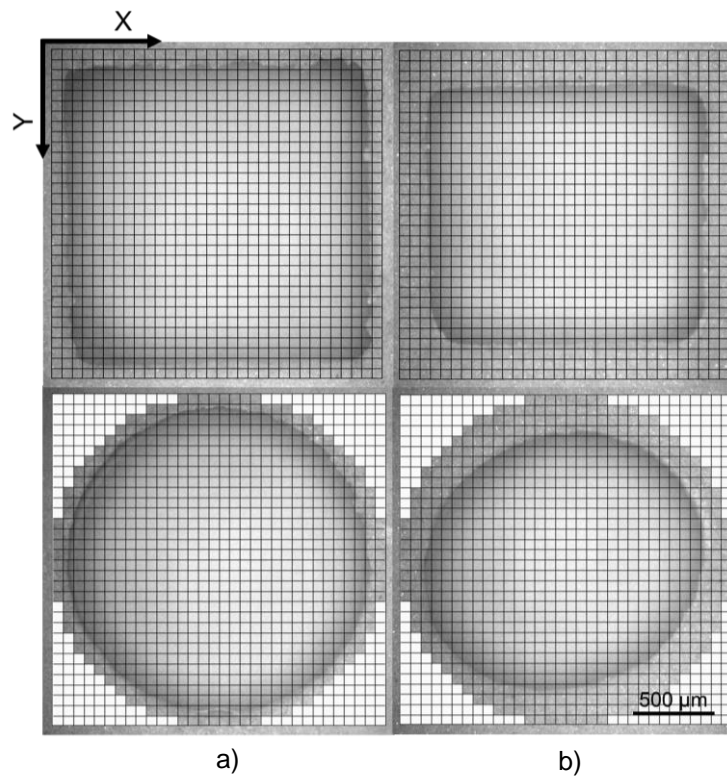
Figure 4.27 - Optical image of the cavities corresponding to the pieces placed in the a) C1 position and b) A5 position.

The cavities corresponding to the C1 piece have ~1.5 pixels less for each side in both axes, with respect to the projected slice. On the other hand, the cavities of the A5 piece have ~3.5 pixels less in the Y-axis in each side, and ~2.5 pixels in the X-axis for each side. Thus, the circular cavities have more circularity in the C1 case than in the A5. Moreover, a broadening of the corners of the quadrangular cavities is observed, which occurs along 2 x 2 pixels (two pixels on the X-axis and 2 pixels on the Y-axis). To conclude, the printing area with higher fidelity is placed in the bottom left of the platform.

Note that the explained results are in terms of pixels, nevertheless the variation is not necessarily dependent on the pixel size, but on the W_{ex} and the 2-3 % of shrinkage of the whole pieces.

4.2.3. Analysis of printing resolution

In this section, the printing resolution is presented for the XY, YZ, and XZ-planes. For this analysis, circular and quadrangular cavities were printed on the surface of these mentioned planes. The CAD model and the resulting printed parts are shown in Figure 4.28, identifying the studied planes.
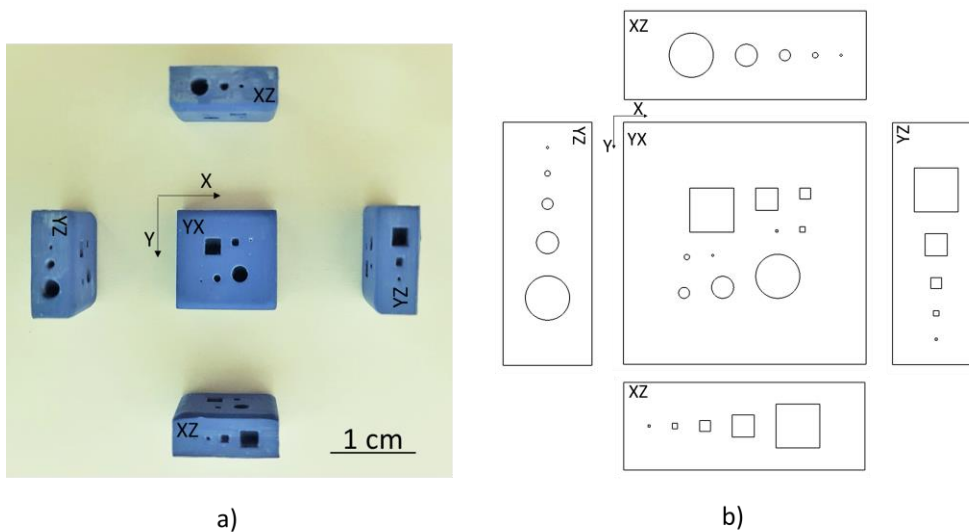
Figure 4.28 – a) CAD images and b) printed pieces with the plane identification

This study was performed in the C1 zone of the printing area, which is the area that has the best results in terms of printing fidelity. The depth of the cavities has the same length of the side/diameter, i.e., an aspect ratio of 1. Table 4.2 shows the dimensions of the designed cavities (side and diameter) and the corresponding number of pixels projected in the XY-plane.

Table 4.2 – Relationship between the defined dimension of the projected pixels and its projected dimension.

Defined dimension (μm)	Number of pixels	Projected dimension (μm)
2000	32	2041.6
1000	16	1020.8
500	8	510.4
250	4	255.2
100	2	127.6

The projected dimension is the number of pixels multiplied by 63.8 µm (size of the pixel). In this regard, the following results consider the projected dimension (slice) and not the defined dimension (CAD). The printing process was performed with h = 25 with an exposure time of 10 seconds.

Figure 29 shows the SEM images of the quadrangular and circular cavities corresponding to the 2000 µm dimensions. In this case the grid has 32 pixel sides and a diameter of 32 pixels for the quadrangular circular cavities, respectively.
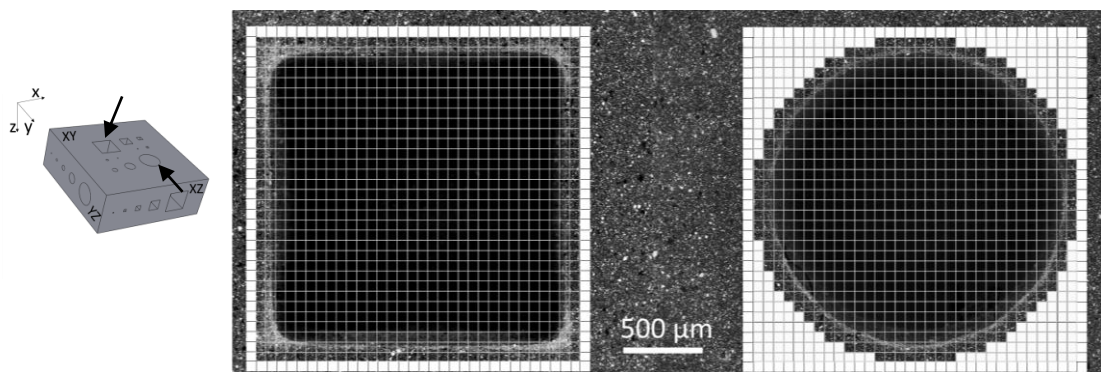
Figure 29 – Quadrangular (left) and circular (right) cavities with 2000 µm side/diameter for the XY-plane.

A deviation of ~ 1.5 pixels in both cavities is measured, so the cavities have smaller dimensions when compared with the projected slice. Moreover, in the quadrangular cavity a higher dimensional variation in the corners is observed, causing its rounding.

Figure 4.30 presents the SEM images of the 1000 µm side/diameter of the quadrangular and circular cavities. The represented grid corresponds to the number of pixels, 16 x 16 pixels, in the case of the quadrangular cavity, and a dimeter of 16 pixels for the circular one.
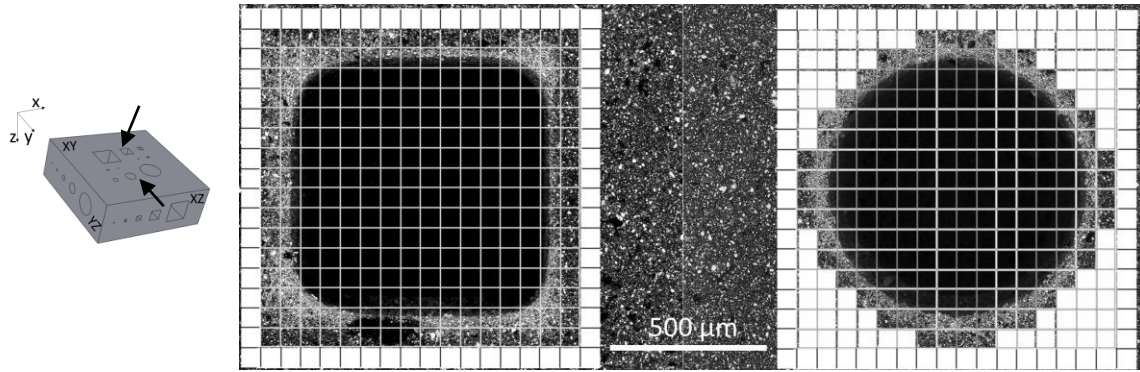
Figure 4.30 – Quadrangular (left) and circular (right) cavities with 1000 µm side/diameter for the XY-plane.

The size reduction is similar to the case of 2000 µm (Figure 29). In this case, the rounding of the corners in the quadrangular cavity is also observed.

In this regard, the whole dimensional variation for the 2000 and 1000 µm geometries is 180 ± 20 µm (twice the W_{ex}). Moreover, in both results the corners of the quadrangular cavities do not have a perfect 90 º. This is explained by the broadening caused by the scattering phenomena. Note that in this area, the contributions of both sides of pixels of the corner are observed, resulting in more scattering. Furthermore, the curvature of the corners occurs along ~2 pixels by side. Thus, in the case of the 1000 µm quadrangular cavity (16 pixels) the straight side is just along ~7-8 pixels because of the scattering and the rounding of the corners.

Figure 4.31 represents both cavities with 500 µm of side/diameter printed on the top of the piece (XY-plane). The presented grid has 8 pixel sides for the quadrangular cavity and 8 pixel diameters for the circular one.
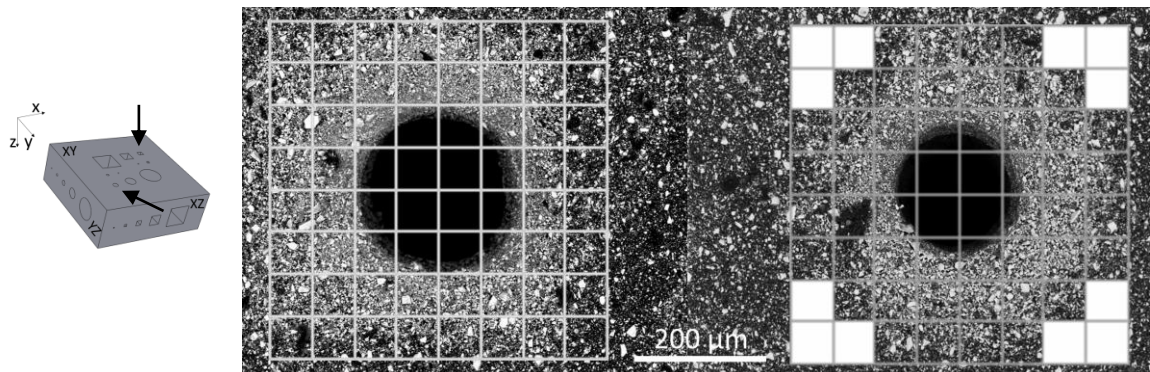
Figure 4.31 – Quadrangular (left) and circular (right) cavities with 500 µm side/diameter for the XY-plane.

The total dimensional variation (twice W_{ex}) for this case has a higher value than the 2000 and 1000 µm cases. The variation in this case is 300 ± 20 µm, with respect to the projected one (510.4 µm). W_{ex} should be a geometrical independent constant, nevertheless it seems to be higher for smaller cavities. This effect is due to the edge contribution.

On the left of Figure 4.31, the quadrangular cavity shows a circular geometry. This is explained by the rounding of the corners. The curvature of the corners and the dimensional deviation are almost constant in previous results (2000 and 1000 µm geometries), around 2 x 2 pixels in each corner. By reducing the side of the quadrangular geometry to 8 x 8 pixels, the printed geometry is reduced to 5/4 pixels side, due to the W_{ex}. Thus, if the curvature of the corner is along 2 pixels, the straight side zone is reduced to zero, connecting the curvatures of the corners. In this regard, the printed geometry seems like a circular cavity.

For the other cavities, i.e., for the ones with dimensions of 250 and 100 µm, the printed cavities are not detected, since the W_{ex} is the same order of magnitude as the designed cavities, causing the complete curing of the cavity.

The following results are related with the YZ and XZ-plane resolutions. As described in the introduction of this chapter, the Z-axis resolution is mainly governed by layer thickness. The printing was performed with a layer thickness of 25 µm, thus the number of layers (n) for each cavity is given by the division of the length/diameter of the geometry by the layer thickness (h). Table 4.3 shows this relationship for all dimensions of the cavities. Note that

the printed cavities present an aspect ratio of 1, thus, the depth is the same as the length/diameter of the cavity.

Table 4.3 – Relationship between defined dimension and the number of layers.

Defined dimension (µm)	Number of layers
2000	80
1000	40
500	20
250	10
100	6

In this section, the results are presented comparing the cavities with the same shape in both the XZ and YZ planes. A frame is presented in all analyses, representing the designed geometry with the corresponding size of layer thickness. The first printed layers are placed at the bottom of the image.

Figure 4.32 shows the SEM images of the cavities with 2000 µm side, printed on the XZ-plane on the left and YZ-plane on the right.
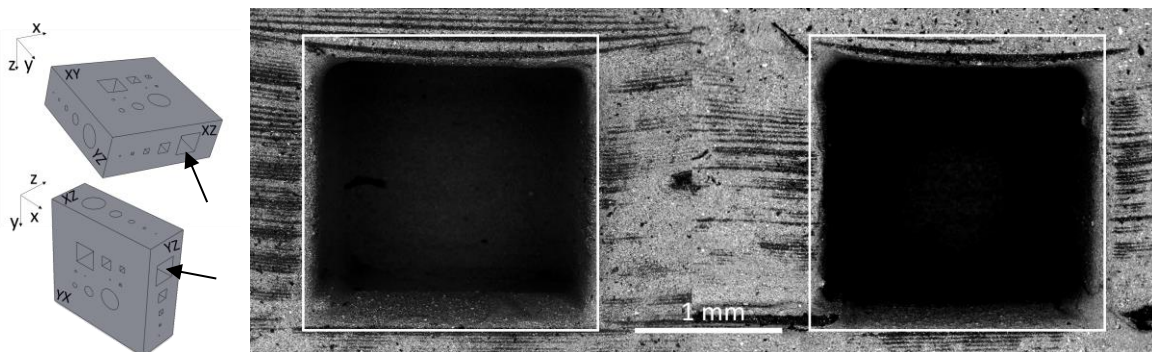

Figure 4.32 – SEM images of the quadrangular cavities in the XZ-plane (left) and YZ (right) with 2000 µm side.

In both cases there is a bending of the top layer of the cavity. This is a defect inherent to the printing technology and depends on the resin formulation and/or the applied energy dose.

During the printing, all cavities are filled with uncured resin, a liquid medium, thus the top layer was cured without a previous cured resin. This effect induces the bending of the layer and, as the cure depth is higher than the printing layer, the cured layer has the maximum cured depth (in this case around 150 µm). This effect is known as print-through. This effect could be controlled by tuning the applied energy dose; the lower the energy dose the lower the print-through. Regarding the width of the cavities, there is a slight dimensional variation in this case, due to the W_{ex} in the X and Y-axes.

Figure 4.33 displays the SEM images of the quadrangular cavities with 1000 µm side, printed on the XZ-plane on the left and YZ-plane on the right.

Figure 4.33 - SEM images of the quadrangular cavities in the XZ-plane (left) and YZ (right) with 1000 µm side.

In this case the bending effect is not so evident as in the previous one. As the width decreases, this effect is reduced due to the shorter distances between the supported walls. However, the contribution of the cure depth is inherent to the process itself.

Regarding the dimensional variation of the whole cavities, it is complicated to evaluate with accuracy due to the rounded perimeter. Nevertheless, the Z-axis (height) variation is around 17 % less than the defined dimensions, in both axes. On the other hand, a dimensional reduction of 12 % is observed for in the X or Y-axis (width). As said before, the X and Y-axis variation corresponds to the W_{ex}.

Figure 4.34 presents the SEM images of the quadrangular cavities of 500 µm side for both the YZ and XZ planes.

Figure 4.34 - SEM images of the quadrangular cavities in the XZ-plane (left) and YZ (right) with 500 µm side.

As in the previous cases, it is observed that the cavities present a smaller dimension than defined ones, where the Z-reduction is caused by the print-through effect and the Y and X-direction due to the W_{ex}.

In all cases analyzed, the corners of the quadrangular cavities do not have a 90° angle. Besides, the rounded perimeter is also a characteristic of all quadrangular cavities and it is independent of the cavity dimension.

The following results represent the circular cavities printed on the YZ and XZ planes (Z-direction). Figure 4.35 shows the SEM images of the circular cavities with a diameter of 2000 µm printed on the XZ-plane on the left and YZ-plane on the right.
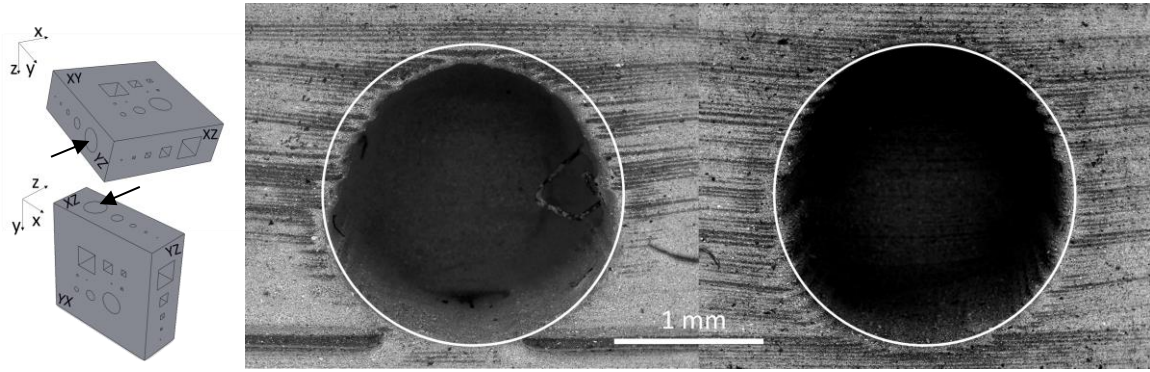
Figure 4.35 - SEM images of the circular cavities in the XZ-plane (left) and YZ (right) with 2000 µm diameter.

The YZ-plane printed cavity has higher accuracy than the XZ-plane. In both cases there is some layer displacement, mainly in the upper half of the circumference.

Figure 4.36 displays the SEM images of the circular cavities with 1000 µm diameter printed on the XZ-plane on the left and YZ-plane on the right.
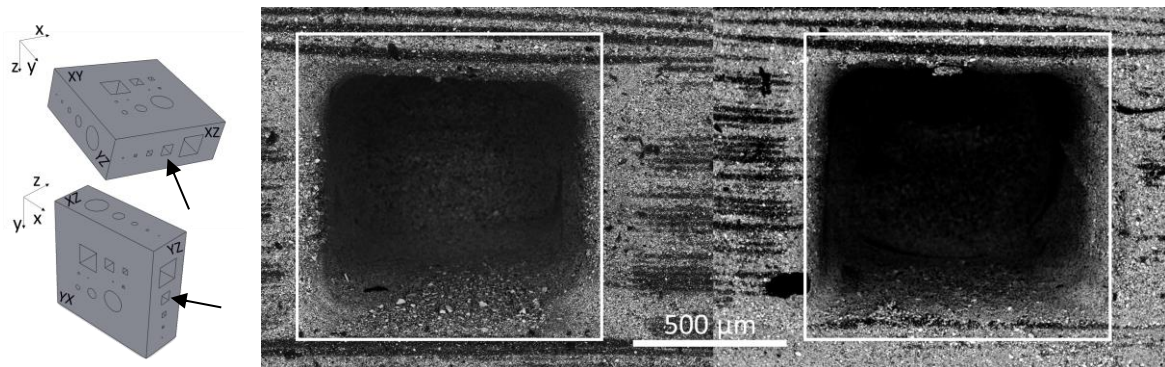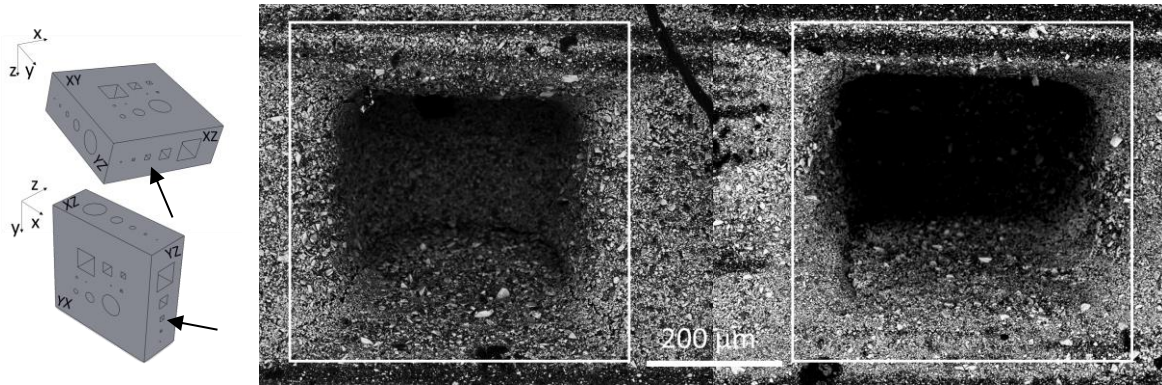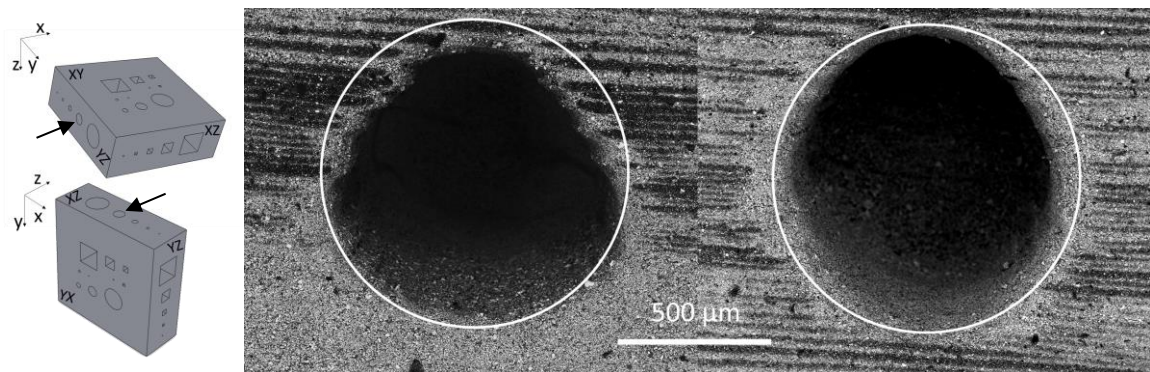

Figure 4.36 - SEM images of the circular cavities in the XZ-plane (left) and YZ (right) with 1000 µm diameter.

As in previous cases, the YZ-plane cavity results in a higher accuracy than in the XZ-plane, and the displacement of the upper layers is not so evident.

Figure 4.37 displays the SEM images of the circular cavities corresponding to a diameter of 500 µm.

151
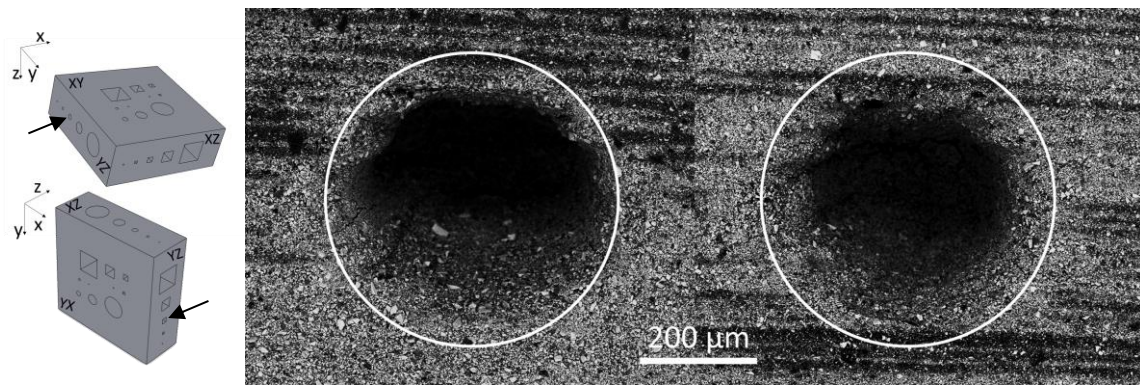
Figure 4.37 - SEM images of the circular cavities in the XZ-plane (left) and YZ (right) with 500 µm diameter.

A higher deformation of the cavity is observed on the XZ-plane. On the other hand, in the YZ-plane the printing of the cavity results in a higher accuracy. In this last case, the dimensional variation presents a 31 % reduction from defined dimensions, from a diameter of 500 to 345 µm. The dashed line on the YZ-plane image represents the printed diameter.

Nevertheless, the higher accuracy in the YZ-plane was not observed for the quadrangular cavities. In this sense, a correlation between geometry accuracy versus XZ or YZ-axes was not completely demonstrated.

Regarding the geometries with smaller dimensions, 250 and 100 µm, it is observed that these geometries are not printed properly.

Figure 4.38 shows the SEM image results of the cavities with 250 µm; on the left the resulting pattern for the quadrangular geometry is presented; on the right the resulting pattern for the circular one is presented, for the YZ-plane.
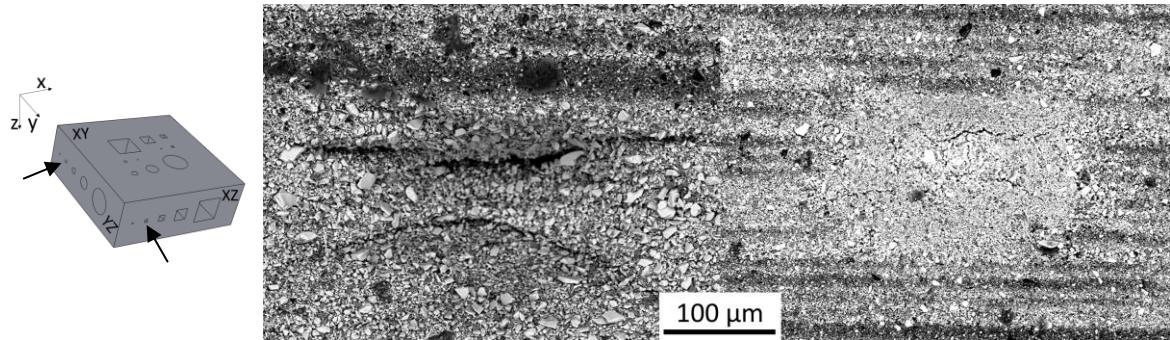
Figure 4.38 – SEM images of the quadrangular (left) and circular (right) cavity with a side/diameter of 250 µm.

As the aspect ratio of the cavity is 1, the theoretical depth in this case is 250 µm. Nevertheless, as the light scattering affects both the X-axis and Y-axis, the depth is also affected. As mentioned in the analysis of the XY plane, the W_{ex} is around 150 µm for the cavities with 500 µm side/diameter. In this sense, as the W_{ex} is close to the defined geometries the cavities are not well reproduced.

For the samples with 100 µm side/diameter, no evidence of their printing was detected when analyzed by SEM imaging.

Figure 4.39 shows a schematic of how the W_{ex} affects the dimension of the cavities printed on the XY-plane and on the XZ-plane (and its equivalent YZ).
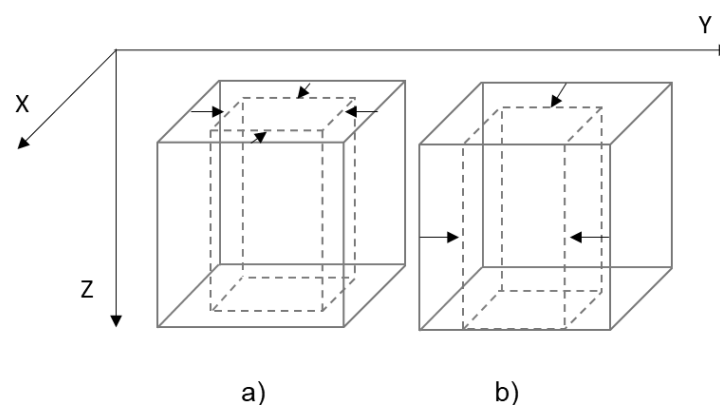
Figure 4.39 – Schematic of the excess width with cured resin by the light scattering in a a) top cavity (XY-plane) and b) lateral cavity (XZ and YZ-plane).

153

To conclude the analysis, the light scattering by the ceramic particles affects the XY resolution, reducing the size of the cavity in both the X and Y-axes. On the other hand, the Z-axis is not affected in this way. Nevertheless, this axis is affected by the print-through effect, which is dependent on the maximum cure depth of the ceramic suspension for the applied energy dose.

The minimum well-defined cavity dimension in the XY-plane is 500 µm for the circular cavities and 1000 µm for the quadrangular ones. The rounding of the corners is present in all quadrangular cavities printed in the XY-plane, limiting its resolution. This effect could be minimized by adjusting the energy dose applied in the corners.[1]–[3], [15]–[17]

 On the other hand, in the Z-directions, the smaller well-defined cavity is the one with 500 µm side/diameter, independent of the geometry.

These results could be improved by reducing the energy dose applied during the printing, nevertheless during the debinding and sintering process some delamination defect could appear, due to the worsened bonding between the layers if the energy dose is not enough. However, the results are within the reported ones. [18]–[21]

4.3. Printing defects

There are so many factors which contribute to the successful printing of the green body. Apart from the ones previously presented, focused on the characteristics of the suspensions and the printing process itself, there are other important parameters which must be considered. In this section, viscosity of the suspension, air bubbles, particle size and agglomerates, sedimentation of the LTCC particles, superficial tension, and some mechanical issues which could occur during the printing process are analyzed and discussed.

As expected, the defects formed during the printing process can increase the internal stress and the distortion on the green body, increasing the difficulty of the thermal treatment of debinding and sintering, performed after the printing process to obtain the final ceramic part. This analysis of the defects also provided crucial information for the LTCC suspension optimization.

4.3.1. Viscosity and recoating system

As said previously, the recoating is composed of three different steps, shown in Figure 4.2, which is associated with a certain time (equation 4.1).

(1) The first step is to lower the platform with a Z-displacement of around 2-3 mm (down position), waiting a certain time to allow the wetting of the green body by the uncured resin ($t_{wetting}$).

(2) The second step is to rise the platform with a certain Z-displacement with respect to the previous Z-position, in function of the layer thickness ($t_{leveling}$).

(3) And the last step is to wait a certain time for the relaxion of the suspensions (t_{wait}).

In this study the LTCC suspension has a viscosity of 12 Pa·s at 2 s^{-1} which is higher than the reported values (viscosities lower than 5 Pa·s at 2 s^{-1}) for this type of recoating system. To evaluate the influence of the viscosity on the recoating of the layers, a tape of 35 x 30 mm was used.

Figure 4.40 shows the recoating defects generated during the printing due to the high viscosity value of the ceramic suspension.
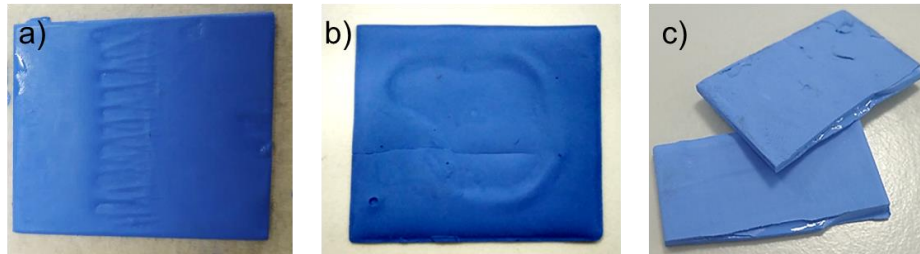
Figure 4.40 – Recoating defects due to the high viscosity.

Figure 4.40.a shows a non-homogeneous layer with a generated defect in the direction of the leveling step, i.e., parallel to the wiper movement. Figure 4.40b represents the defect of wetting of the surface, where the flowability of the ceramic resin is not appropriate for the recoating of the whole surface of the tape. Due to the non-uniformity of the recoating, the tape has some uncured resin inside the piece, shown in Figure 4.40c. This defect could be improved by lowering the platform a higher distance than the applied one and wait more time in the down position to compensate for the lack of flowability. However, it is convenient to work with a suspension with lower viscosity. In this regard, to ensure a good flowability, the optimized LTCC suspensions should have a viscosity lower than the reported one, around 3.6 Pa·s at 2 s^{-1}, resulting in a proper recoating process, as shown in Figure 4.41.

Figure 4.41 – Recoating layer of the optimized LTCC suspension.

4.3.2. Air bubbles in the LTCC suspension

During the fabrication of the LTCC suspensions the formation of air bubbles is inherent to the process itself, since the movement of the balls during the dispersion procedure in the ball milling or removing the balls from the ceramic suspension generate air bubbles in the suspension. Apart from this, during the printing process, the formation of air bubbles is also possible due to the platform movements. Even with the wiper system, which aids in the homogenei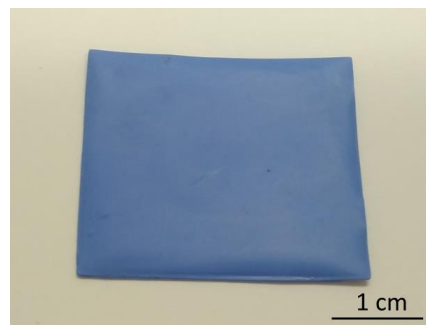ty of the resin surface, if the air bubbles are too stabilized, their elimination could be not successfully achieved by this system.

In this regard, an antifoam was added to the LTCC suspensions as explained in the previous chapter. Figure 4.42 shows the improvement of the formulation by adding the antifoam. Figure 4.42.a shows a LTCC suspension without the antifoam additive where the air bubbles are quite evident. However, by adding this organic additive the resin is free of air bubbles, as observed in Figure 4.42b.
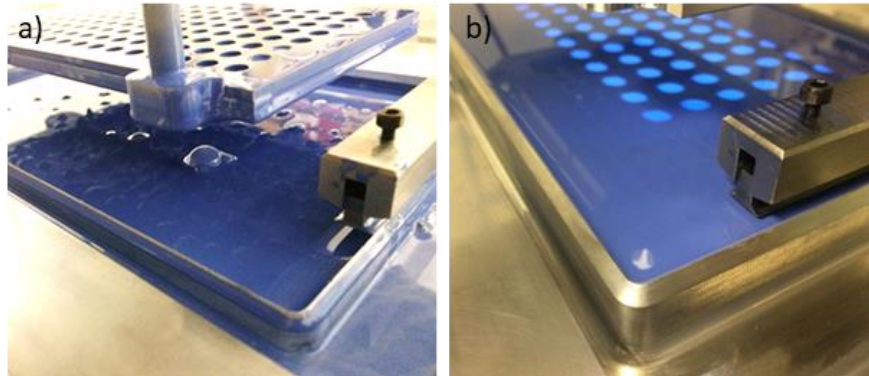
Figure 4.42 – Effect of the antifoam on the LTCC suspension formulation: a) LTCC suspension without antifoam and b) LTCC suspension with 0.4 wt.% of antifoam with respect to the total weight.

If the LTCC suspension has air bubbles, the printed pieces will also have these defects which cannot be eliminated, resulting in voids on the final ceramic pieces. Figure 4.43a shows a green piece printed with a formulation without the antifoam, and the final result after the sintering process in Figure 4.43b.
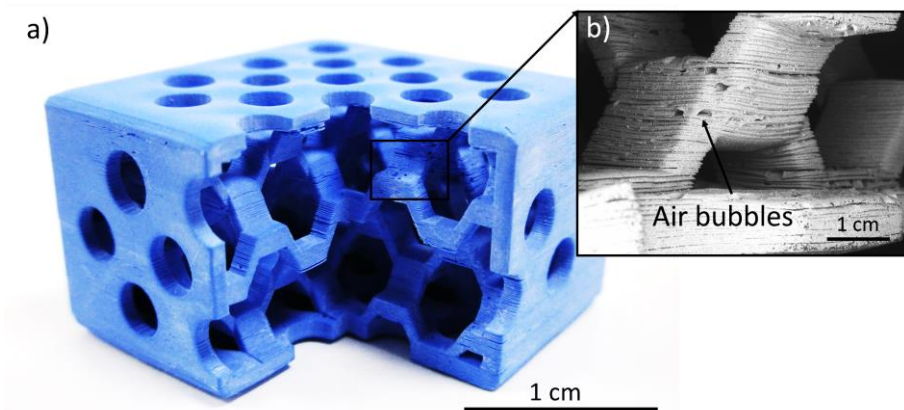
Figure 4.43 – Air bubbles defect present in the a) green piece and b) after the sintering process

Once the air bubble defect is generated, the defect will be on the final sintered piece, worsening the mechanical properties. Besides this defect, the delamination of the layers is also observed which is another defect further discussed in the next chapter.

4.3.3. Sedimentation

The stabilization of the ceramic suspensions is also a key factor for homogenization of the printed pieces. As the LTCC powder has different particle size and densities, the sedimentation process occurs differently depending on the particle's characteristics. In this regard, two different situations are presented: on one hand, the influence of the viscosity and its effect on the sedimentation of the powder, and on the other hand, a slight separation of fine particles from the whole suspension.

Two processes were observed regarding the particle sedimentation (Figure 4.44). In Figure 4.44.a, a substantial sedimentation of the LTCC powder on the bottom of the printer vat is observed and in Figure 4.44.b, some slight floating of small particles can be detected.
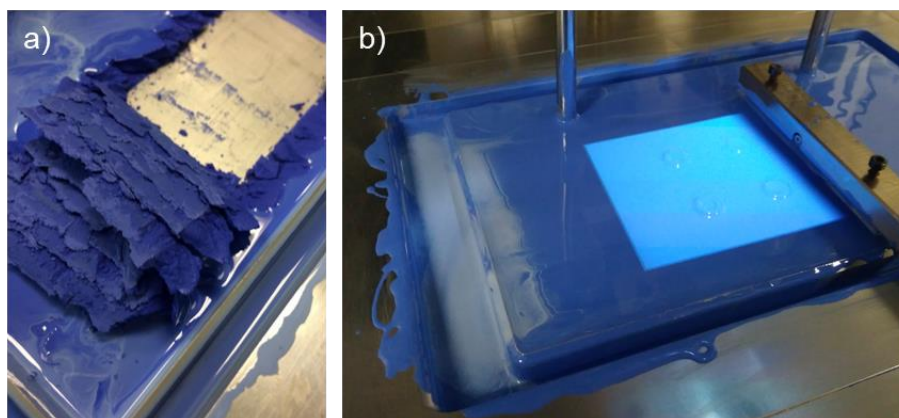
Figure 4.44 – Images of a) sedimentation of the LTCC particles on the bottom of the vat - high sedimentation rate - and b) floating of small particles at the suspension surface - white zones.

To better understand the sedimentation of the particles, due to the viscosity, two kinds of dispersant were used: DISPERBYK-2013 to reach really low viscosities and the Multitrope 1214 to achieve the optimal formulation of the LTCC suspension. Regarding the high rate sedimentation (Figure 4.44.a), the LTCC suspensions loaded at 67 wt.% were studied at different DISPERBYK-2013 concentrations. Figure 4.45a presents the flow curves vs. dispersant concentration, with respect to the solid load, and Figure 4.45.b shows the viscosities at 2 s^{-1} for the different concentrations. Note that in Figure 4.45.b not all the concentrations are presented.
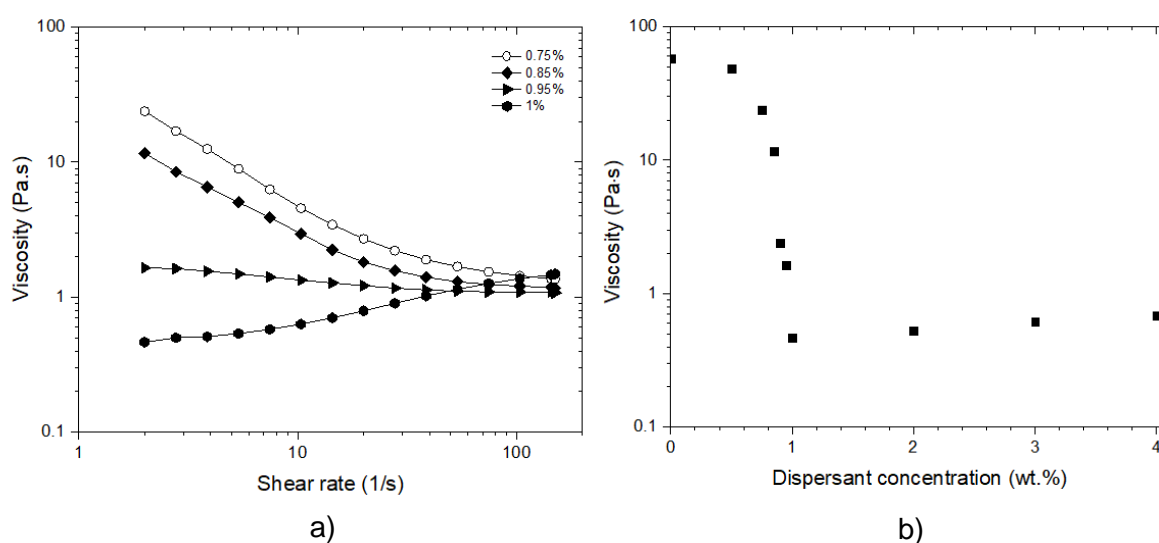
Figure 4.45 –a) flow curves for different dispersant concentrations b) viscosity vs. dispersant concentration (DISPERBYK-2013) at a shear rate of 2 s^{-1}.

The addition of the dispersant drastically decreases the viscosity of the LTCC suspensions, reaching a minimum at 1 wt.%, as seen in Figure 4.45b. The viscosity of this formulation is 0.5 Pa·s at a shear rate of 2 s^{-1}. Moreover, as observed in Figure 4.45a, this formulation presents a dilatant behavior, which means that at zero shear rate the viscosity of the suspensions is very low. Thus, both low viscosity and dilatant behavior lead to the rapid sedimentation of the ceramic particles. As expressed by the Stokes' law, the sedimentation velocity is inversely proportional to the viscosity. Moreover, by increasing the sedimentation rate, the LTCC suspensions could not be used for long periods of time. Thus, it was decided to work with the Multitrope 1214 dispersant, because it does not produce such abrupt viscosity and rheological behavior changes.

In the optimized LTCC suspension with the Multitrope 1214 dispersant some slight floating of the particles was detected, the white zone seen in Figure 4.44b. For the analysis, the interface of the blue and the white suspension was cured for a more accurate analysis by SEM imaging. Figure 4.46a shows the powder morphology at the interface of both zones.
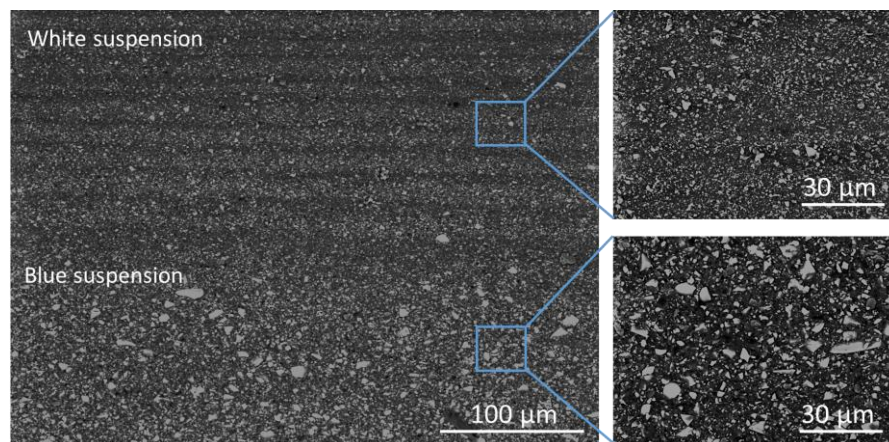
Figure 4.46 – Particle size distribution of the white and blue zones.

A particle size gradient is observed along the SEM image. The upper part and the bottom part of the image corresponds to the white and blue areas, respectively. A clear difference in terms of particle size distribution between the white and the blue zone is detected. In the case of the white area, the particle size is smaller in comparison with the blue zone. This occurs due to the low weight of the small particle, which tends to float.

The change in terms of color could be associated to the presence of cobalt (II) aluminate ($CoAl_2O_4$), which has a blue color. In this regard, the white zone does not have the same concentration of the oxide, changing its color from blue to white. However, it was observed that these fine particles can be easily re-dispersed. Therefore, this phenomenon is not a drawback for the process.

4.3.4. Particles size and agglomerates

As explained in the previous chapter, the particle size distribution takes an important role not just in the photopolymerization behavior but also in avoiding printing defects. If the ceramic suspension has particles with a higher size than the layer thickness, the green body will contain some inhomogeneities between layers.

Figure 4.47.a displays a green body printed with a LTCC suspension fabricated by mechanical stirring, i.e., without further dispersion using a ball milling process.
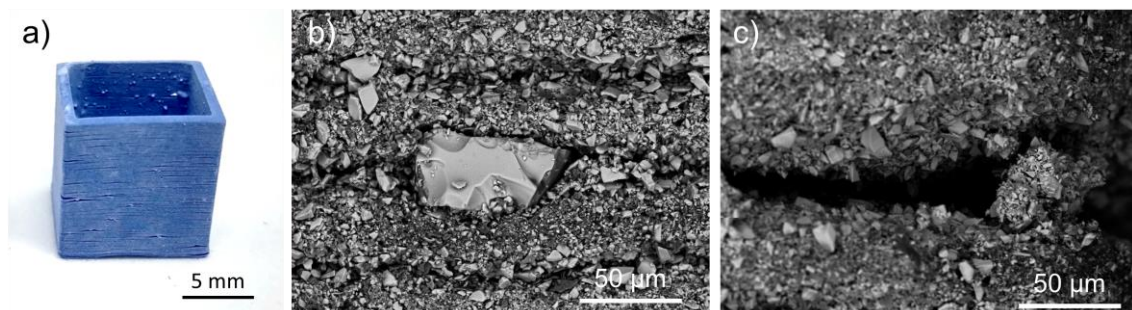
Figure 4.47 – a) Green body printing with a non-well-dispersed LTCC suspension, b) the generated defect due to the particle size, and c) the generated defect due to the particle agglomerations.

As observed in Figure 4.47a, the green body presents a non-homogeneous surface with visible delamination between layers. Figure 4.47 shows SEM images of the defect present between layers, caused by large particles, Figure 4.47b, and agglomerates, Figure 4.47c.

This result shows the importance of a good homogenization of the LTCC suspension, to avoid the defect formation during the printing process. In fact, the value of d_{50}, i.e., the diameter at which 50 % of a sample's mass is comprised of smaller particles, is a crucial parameter for

the formulation of the suspension. However, the value of the highest particle size present in the ceramic suspensions is also important, because if the maximum particle or agglomerate size is higher than the printed layer thickness, this kind of defect can appear on the green body. In this regard, a dispersing process using a ball milling system, for example, is convenient for the deagglomeration of the particles and a slight reduction of the particle size, as seen during the optimization of the LTCC suspension.

4.3.5. Out of plane defect and surface tension

In a top-down MIP-SLA configuration, the photopolymerization occurs at the suspension surface, thus, a smooth and flat surface is required for a proper printing process. Thus, as the printing process is performed at the air-liquid interface on a cured layer, some surface tension effect is observed on the perimeter of the cured pieces. As a result of the surface tension, the liquid LTCC suspension tends to shrink into the minimum surface area possible. This means that at the solid (cured layer) to liquid interface (uncured resin), the formation of a curvature is observed. [3], [10]

Figure 4.48 shows this out of plane defect. This printing defect is clearly observed once the printed piece is out of the resin level (dashed white line).
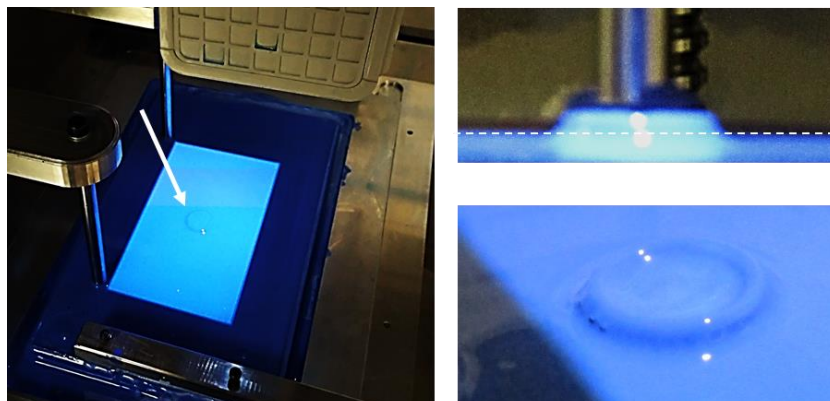
Figure 4.48 – Out of plane defect during the printing process.

Two different hypotheses justify this effect; 1) the resin level is not kept constant along the printing process due to the wiper movement which might pour out too much resin into the surrounding channel and 2) the effect of the surface tension of the uncured resin on the cured one. If the level of the resin is decreasing during the printing, the printed pieces will have a lower layer thickness on the top. Nevertheless, during the analysis of the printed pieces no significant differences on the layer thickness were detected. Thus, the first hypothesis is discarded.

Therefore, the presence of the out of plane defect is due to the surface tension of the system. The following characterization is focused on the top of the printed cylinders with different layer thicknesses, for a deeper analysis of this defect.

Figure 4.49 shows the SEM images of a cross section of these cylinders, displaying the curvature on the top of the printed parts in all cases.
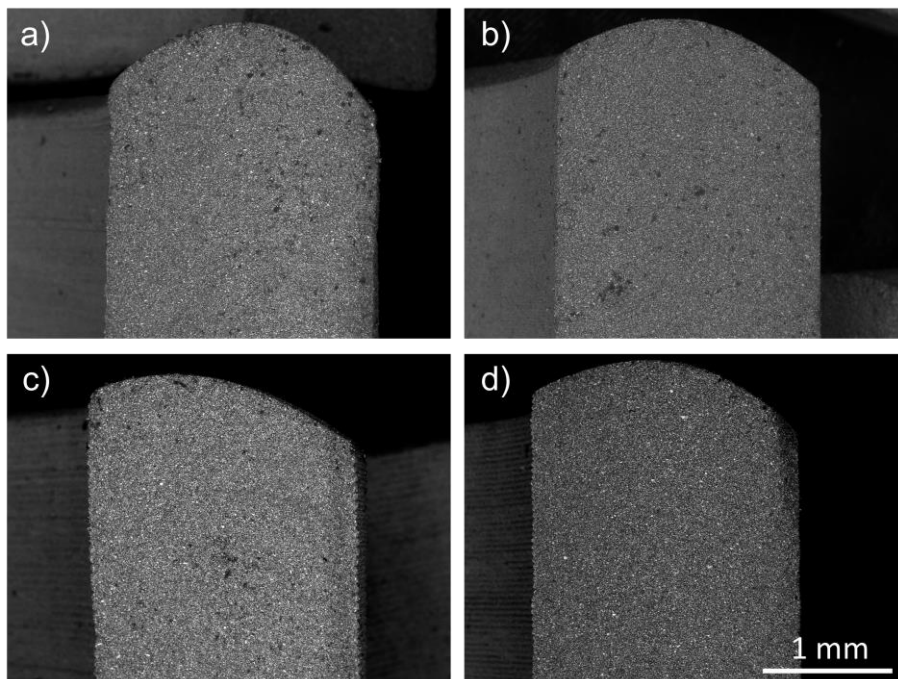
Figure 4.49 – Cross section of the pieces printed with different layer thicknesses a) 12.5 μm b) 25 μm c) 50 μm and d) 75 μm, with the same magnification.

Figure 4.50 shows a diagram of the superficial tension effect observed during the printing process. Figure 4.50a represents an ideal situation, where the cured layers are the same level as the uncured suspension level. On the other hand, Figure 4.50b shows the effect of the surface tension during the printing process, which results in the curvature of the pieces with a certain variation in the Z-direction (ΔZ_{ST}).
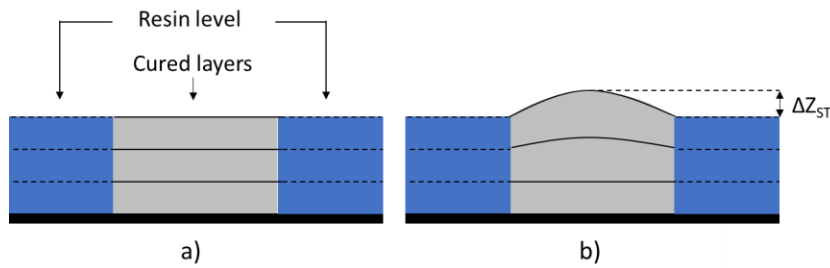
Figure 4.50 – a) ideal situation and b) effect of the surface tension on the overgrowth of the printed pieces.

In an extreme overgrowth of the pieces, the wiper impacts the printed pieces during the leveling of the suspension, causing more defects on the green body.

Figure 4.51 shows the defect generated by the wiper when the part has an excessive overgrowth.
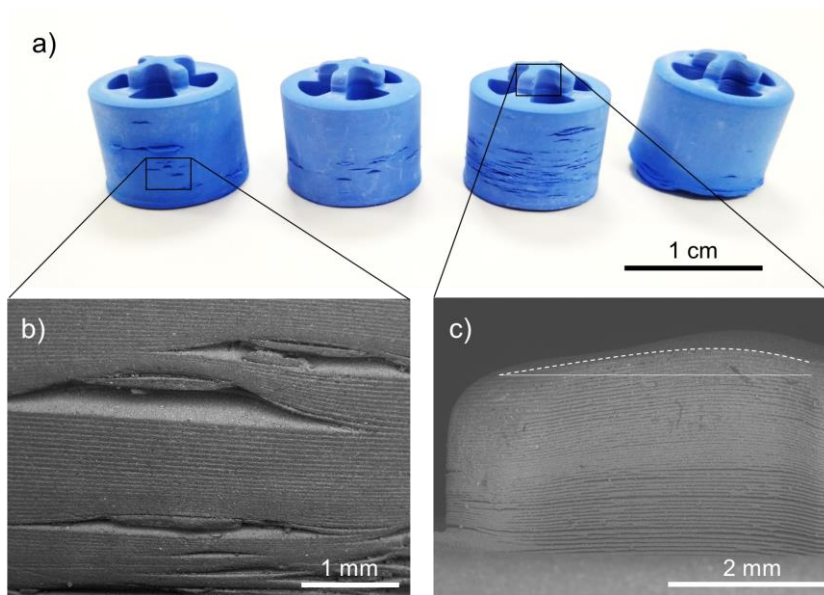
Figure 4.51 – a) Green bodies and SEM images of the b) wiper defect and c) overgrowth of the green piece.

This effect is inherent to the technology itself and is also reported for resins without ceramic particles. Therefore, it cannot be avoided but it can be minimized. The amplitude of the curvature can be improved during the recoating step, by increasing the so-called t_{wait}, giving time for the resin to level.[22] Another strategy is to print the pieces with a certain inclination, changing the CAD model and adding some printing supports. In this way, if the last layers have a lower surface, this effect is minimized.

4.3.6. Adhesion between layers

The following defect is caused by the poor adherence of the first layers on the platform. In the case that the green body is not well attached to the platform, the piece could move during the printing process. Figure 4.52 shows two examples caused by this effect.

a)   b)
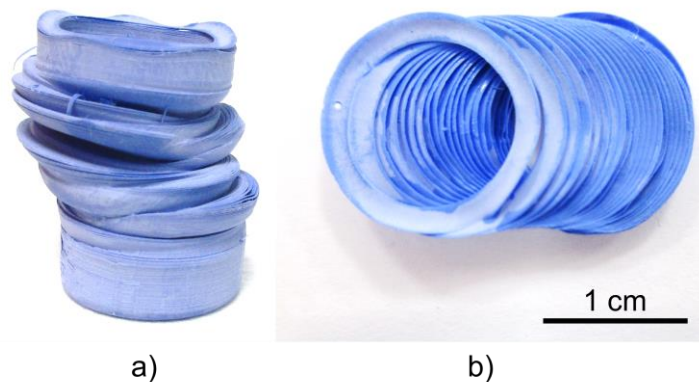
Figure 4.52 – Examples of green bodies which were not well attached to the building platform.

To avoid this issue two strategies were applied: 1) a higher energy dose must be applied on the first layers and 2) a thin layer of SPOT-LV resin is cured on the platform. Nevertheless, if the pieces are too attached to the platform, the removal of the pieces is harder and could induce some defects on the printed parts.

4.4. Comparison of vat-photopolymerization printers

In this section, a comparison of AM printers of ceramic materials, based on the vat-photopolymerization process, is presented. This comparison will consider the printing velocity, resolution, and printing area to evaluate the obtained result with the state-of-the-art.

For this analysis, the time spent printing each layer is calculated considering the optimized printing conditions for the LTCC suspension. The build time scale with the number of layers, since each layer requires a certain time for the recoating and for the polymerization process. Based on equation 4.2, the established experimental conditions result in a total time of 40 seconds per printed layer, translating to 90 slices per hour:

$$t_{layer} = 8 + 18 + 4 + 10 = \ 40 \ s \ /layer$$

As previously mentioned, the MIP-SLA machine used in this work was developed within the scope of the NHIBRID project, thus the MIP-SLA machine is called NHIBRID. Table 4.4 shows the summary of the features of the NHIBRID machine taking into consideration the established conditions during the printing tests.

Table 4.4 – Features of the Hybrid AM machine developed and used in this work.

Company	AM machine	Layer thickness (µm)	XY resolution	Printing velocity	Printing area (mm)
F-CIM	NHIBRID	>25 - <150[1]	1920 x 1080 px (63.8 µm)	90 Slices/h	122.5 x 68.9 x 30 (X,Y,Z)

(1)   The maximum will depend on the ceramic suspension formulation and the exposure time.

Table 4.5 shows the features of commercial AM ceramic printers based on the vat photopolymerization process for further comparison.

Table 4.5 – Benchmarking of commercial SLA/MIP-SLA ceramic AM machines.

Company	AM machine	Layer thickness (µm)	XY resolution	Printing velocity	Printing area (X,Y,Z)
3Dceram	CERAMAKER 100	10-125	30 µm (laser spot)	50 slices/h[1]	100 x 100 x 100
	CERAMAKER 900				300 x 300 x 100
Admatec	ADMAFLEX 130	25 – 100	1920 x 1080 px (50 µm pixel)	20-25mm/h	96 x 54 x 120
Prodways	ProMaker V6000	25 - 150	1920 x 1080 px (32 µm pixel)	-	120 x 500 x 150
Lithoz	CeraFab 7500	10-100	1920 X 1080 px (40 µm)	100 slices/hour	76 x 43 x 170
	CeraFab 8500		1920 X 1080 px (60 µm)		115 x 64 x 200

(1)   Experimental data from IREC (Institut de Recerca en Energia de Catalunya)

Regarding the Z-resolution, the 3DCeram and Lithoz printers allow for higher resolutions than the Admatec, Prodways, and NHIBRID printers. However, the Z-resolution obtained for the NHIBRID printer is the same given by the Admatec and Prodways printers, with a minimum layer thickness of 25 µm.

With respect to the XY resolution, in the case of MIP-SLA technologies, used by Admatec, Prodways, and Lithoz, this value can be tuned by the distance of the light source. In this sense, all printers based on this technology could achieve similar resolutions. As the printing area in these cases is given by the distance of the light source, both the XY-resolution and printing area are correlated. The way to increase the printing area without losing XY-resolution is to have a multi light source or to move the light source during the printing process. This last case is present in the Prodways printer, which allows for printing higher areas with high resolution. On the other hand, the SLA technology of 3DCeram presents the highest printing area with the highest resolution, once the laser could scan a higher area guaranteeing a high resolution along the whole area.

With respect to the printing velocity, it is observed that in the MIP-SLA technologies a higher printing velocity could be obtained. This is due to the printing process itself: each layer is printed at the same time and not point by point as in the SLA-based technology (3DCeram printers). The printing velocity obtained for the NHIBRID printer is 90 slices per hour, which is similar to that reported by Lithoz.

Analyzing the commercial AM ceramic machines, it could be concluded that in terms of AM machine features, the NHIBRID characteristics are within those of the commercially available machines.

For example, some complex geometries were successfully manufactured (shown in Figure 4.53), demonstrating the feasibility of the developed LTCC suspensions for the NHIBRID printer.
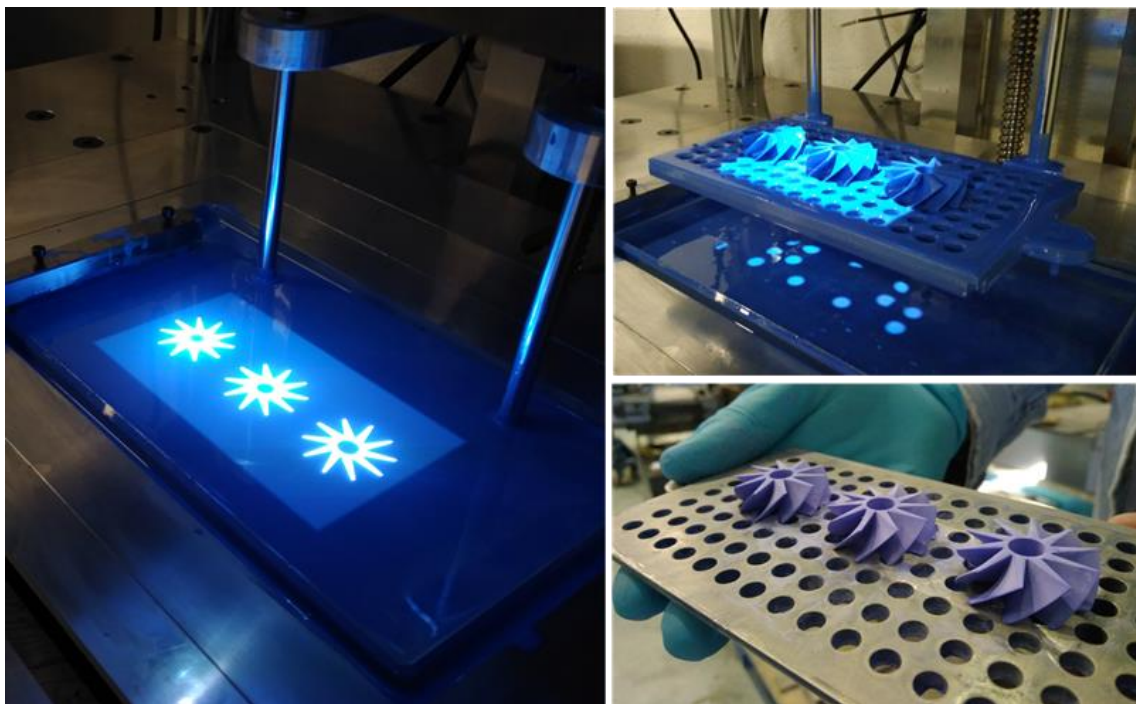

Figure 4.53 – Printing of complex geometries using the NHIBRID printer.

Conclusions

In this chapter, the printability features of the optimized LTCC photocurable suspension were studied regarding the influence of the layer thickness, the printing area, and the resolution in the XY-plane and Z-direction.

The printing process was performed at different layer thicknesses while maintaining the applied energy dose, demonstrating that the printed pieces do not present delamination between layers. Moreover, excellent accuracy was obtained in the Z-direction for the layer thicknesses of 25, 50, and 75 µm. However, an overgrowth of 10 % was detected in the Z-direction due to the surface tension.

The studies summarized in this chapter provide conclusive evidence that the shrinkage of the printed pieces presents significant differences in the X and Y-axes. It was demonstrated that the shrinkage in the X-axis is 1.8 ± 0.8 % and the shrinkage observed for the Y-axis is 2.9 ± 0.7 %.

Moreover, the excess width in the XY-plane is not uniform along the printing area and presents different values on both axes. It was demonstrated that the X-axis presents less excess width than in the Y-axis. In the X-axis the variation of the excess width is 90 µm along the printing area, however the excess width in the Y-axis is 166 µm. Likewise, the values of the excess width are higher in the Y-axis than in the X axis, with values ranging between 50-215 µm and 60-150 µm, respectively.

Regarding the fidelity of the patterns over the printing area, the experiments demonstrate that the worst results are placed where the difference between the dimensional variation in the X-plane and the Y-plane is greater, considering both excess width and shrinkage.

As expected, it was proven that the excess width does not affect the accuracy in the Z-axis. However, in all axes the effect of rounding of the perimeters was observed for the cavities printed in all the planes (XY, XZ, YZ). Nevertheless, in the ZX plane and ZY plane, the patterns are reduced by the excess width, but not the height of the cavities. Regarding the Z-direction, the geometry is affected by the print-through effect, mainly for the quadrangular

cavities. Thus, the minimum detail possible to print in the XZ and YZ planes is 500 μm side/diameter, taking into consideration that the printed cavities are reduced by the excess width and height by the print-through effect.

The minimum feature size in the XY-plane is 500 μm for the circular cavities and 1000 μm for the quadrangular ones. As mentioned, the rounding of the corners is present in all quadrangular cavities printed in the XY-plane, limiting its resolution. For patterns above 500 μm, the excess width has the same effects, with a value of 90 μm for the optimized LTCC suspension. On the other hand, for the patterns below 500 μm, the excess width is higher with a value of 150 μm. As the pattern size decreases, the effect of the edges becomes more significant, increasing the excess width (overlapping of energy doses).

In this sense, to ensure a correct pattern transfer of a quadrangular shape the dimensions must be higher than 500 μm in the XY-plane, considering that the corners are rounded if the same energy dose is applied in the 2D image, with a total size reduction of 180 μm. On the other hand, the circular shape could be designed with 500 μm, knowing that the final shape will be reduced to 200 μm.

References

[1]   C. Zhou and Y. Chen, "Calibrating Large-area Mask Projection Stereolithography for Its Accuracy and Resolution Improvements," in *Solid Freeform Fabrication Symposium*, 2019, pp. 82–97.

[2]   C. Zhou and Y. Chen, "Additive manufacturing based on optimized mask video projection for improved accuracy and resolution," *J. Manuf. Process.*, vol. 14, pp. 107–118, 2012.

[3]   T. Hafkamp, G. Van Baars, B. De Jager, and P. Etman, "A feasibility study on process monitoring and control in vat photopolymerization of ceramics," *Mechatronics*, vol. 56, pp. 220–241, 2018.

[4]   T. Chartier *et al.*, "Influence of irradiation parameters on the polymerization of ceramic reactive suspensions for stereolithography," *J. Eur. Ceram. Soc. jo*, vol. 37, pp. 4431–4436, 2017.

[5]   J. W. Halloran, "Ceramic Stereolithography: Additive Manufacturing for Ceramics by Photopolymerization," *Annu. Rev. Mater. Res.*, vol. 46, pp. 19–40, 2016.

[6]   F. Liravi, S. Das, and C. Zhou, "Separation Force Analysis based on Cohesive Delamination Model for Bottom-up Stereolithography Using Finite Element Analysis," in *Solid Freeform Fabrication Symposium*, 2014, vol. 1, pp. 1432–1451.

[7]   Y. Zhang, A. Jariwala, and D. W. Rosen, "Effects of Oxygen Inhibition and Post-Processing on Exposure Controlled Projection Lithography Process Accuracy," in *Solid Freeform Fabrication Symposium*, 2010, pp. 346–359.

[8]   Q. Lian, F. Yang, H. Xin, and D. Li, "Oxygen-controlled bottom-up mask-projection stereolithography for ceramic 3D printing," *Ceram. Int. J.*, vol. 43, pp. 14956–14961, 2017.

[9]   G. Mitteramskogler *et al.*, "Light curing strategies for lithography-based additive manufacturing of customized ceramics," *Addit. Manuf.*, vol. 1–4, pp. 110–118, 2014.

[10]   O. Santoliquido, P. Colombo, and A. Ortona, "Additive Manufacturing of ceramic components by Digital Light Processing : A comparison between the ' bottom-up ' and the ' top-down ' approaches," *J. Eur. Ceram. Soc.*, vol. 39, pp. 2140–2148, 2019.

[11]   C. Bae and J. W. Halloran, "Influence of Residual Monomer on Cracking in Ceramics Fabricated by Stereolithography," *Int. J. Appl. Ceram. Technol.*, vol. 8, pp. 1289–1295, 2011.

[12]   X. Wu, Q. Lian, D. Li, and Z. Jin, "Tilting separation analysis of bottom-up mask projection stereolithography based on cohesive zone model," *J. Mater. Process. Technol.*, vol. 243, pp. 184–196, 2017.

[13]   Y. Pan, H. He, F. Xu, and A. Feinerman, "Study of separation force in constrained surface projection stereolithography," *Rapid Prototyp. J.*, vol. 32, pp. 353–361, 2017.

[14]   S. C. Ligon, R. Liska, M. Gurr, and R. Mülhaupt, "Polymers for 3D Printing and Customized Additive Manufacturing," *Chem. Rev.*, vol. 117, pp. 10212–10280, 2017.

[15]   Y. Chen and R. A. Waltz, "Optimized Mask Image Projection for Solid Freeform Fabrication," in *International Design Engineering Technical Conferences and Computers and Information in Engineering Conference*, 2009, pp. 1–19.

[16]   S. L. Campanelli, G. Cardano, R. Giannoccaro, A. D. Ludovico, and E. L. J. Bohez, "Statistical analysis of the stereolithographic process to improve the accuracy," *Comput. Des.*, vol. 39, pp. 80–86, 2007.

[17]   Y. Lin, M. Chen, and C. Yang, "A Simultaneously Sensing System to Improve Efficiency of Digital Light Process Printing," in *International Conference on Applied System Innovation*, 2017, pp. 1379–1382.

[18]   S. P. Gentry, "PhD Dissertation: Factors Affecting the Resolution of Photopolymerized Ceramics," University of Michigan, 2012.

[19]   T. Chartier, C. Chaput, F. Doreau, and M. Loiseau, "Stereolithography of structural complex ceramic parts," *J. Mater. Sci.*, vol. 37, pp. 3141–3147, 2002.

[20]   E. Schwarzer, M. Götz, D. Markova, D. Stafford, U. Scheithauer, and T. Moritz, "Lithography-based ceramic manufacturing (LCM) − Viscosity and cleaning as two quality influencing steps in the process chain of printing green parts," *J. Eur. Ceram. Soc.*, vol. 37, pp. 5329–5338, 2017.

[21]   U. Scheithauer, E. Schwarzer, T. Moritz, and A. Michaelis, "Additive Manufacturing of Ceramic Heat Exchanger : Opportunities and Limits of the Lithography-Based Ceramic Manufacturing (LCM)," *J. Mater. Eng. Perform.*, vol. 27, pp. 14–20, 2018.

[22] T. Hafkamp, G. Van Baars, B. de Jager, and P. Etman, "A trade-off analysis of recoating methods for vat-photopolymerization of ceramics," in *Proceedings of the 28th Annual International Solid Freeform Fabrication Symposium*, 2017, pp. 687–711.